



Novel cannabidiol–carbamate hybrids as selective BuChE inhibitors: Docking-based fragment reassembly for the development of potential therapeutic agents against Alzheimer's disease



Xia Jiang^{a,1}, Ziwen Zhang^{a,1}, Jiawei Zuo^a, Chengyao Wu^a, Liang Zha^a, Yingying Xu^a, Sheng Wang^b, Jingbo Shi^a, Xin-Hua Liu^a, Jing Zhang^{c,**}, Wenjian Tang^{a,*}

^a School of Pharmacy, Inflammation and Immune Mediated Diseases Laboratory of Anhui Province, Anhui Medical University, Hefei, 230032, China

^b Center for Scientific Research, Anhui Medical University, Hefei, 230032, China

^c Anhui Prevention and Treatment Center for Occupational Disease, Anhui No. 2 Provincial People's Hospital, Hefei, 230041, China

ARTICLE INFO

Article history:

Received 15 June 2021

Received in revised form

8 July 2021

Accepted 28 July 2021

Available online 2 August 2021

Keywords:

Cannabidiol

Carbamate

Fragment reassembly

Acetylcholinesterase

Butyrylcholinesterase

Pseudo-irreversible

Alzheimer's disease

ABSTRACT

Cannabidiol (CBD) and rivastigmine have been launched as drugs for treating dementia and cholinesterases (ChEs) are ideal drug targets. This study focused on developing novel ChE inhibitors as drug leads against dementia through molecular modeling and fragment reassembly approaches. A potent carbamate fragment binding to active site gorge of BuChE was found via a docking-based structural splicing approach, thus, 17 novel compounds were designed by structural reassembly. Compound **C16** was identified as a highly selective potent BuChE inhibitor ($IC_{50} = 5.3$ nM, $SI > 4000$), superior to CBD ($IC_{50} = 0.67$ μ M). **C16** possessed BBB penetrating ability, benign safety, neuroprotection, antioxidant and pseudo-irreversible BuChE inhibition ($K_d = 13$ nM, $k_2 = 0.26$ min^{-1}), showing good drug-like properties. In vivo studies confirmed that **C16** significantly ameliorated the scopolamine-induced cognition impairment, almost entirely recovered the $A\beta_{1-42}$ (icv)-impaired cognitive function to the normal level, showed better behavioral performance than donepezil and good anti-amyloidogenic effect. Hence, the potential BuChE inhibitor **C16** can be developed as a promising disease-modifying treatment of AD.

© 2021 Elsevier Masson SAS. All rights reserved.

1. Introduction

Alzheimer's disease (AD) is an irreversible and severe progressive neurodegenerative disorder [1,2]. In the last few decades, the approved drugs for treating AD include the *N*-methyl-*D*-aspartate receptor antagonist memantine and the cholinesterase inhibitors donepezil, rivastigmine and galantamine, however, they cannot effectively cure this disease, but they do provide short-term symptomatic relief [3]. Two main cholinesterases (ChEs), acetylcholinesterase (AChE) and butyrylcholinesterase (BuChE), are involved in the hydrolysis and regulation of ACh in vertebrates [4]. Various cholinergic drugs, especially BuChE inhibitors also function as AChE inhibitors, while the use of high selective BuChE inhibitors

including MF-8622 and cymserine indicated the potential therapeutic benefit of inhibiting BuChE in AD and related dementias [5–8]. BuChE activity progressively increases as the severity of dementia advances, while AChE activity declines, therefore, inhibition of BuChE may provide additional benefits. Hence, BuChE was considered as an important target for novel drug development to treat AD, and the development of BuChE-specific inhibitors could lead to improved clinical outcomes in the future [9–20]. Moreover, oxidative stress caused by free radicals has been proved to be the main factor leading to the development of AD. Therefore, BuChE inhibitors with the antioxidant potential may have a special therapeutic effect on AD [21–23].

Etiological research implicated cannabis use as a risk factor for psychotic illness in general and schizophrenia in particular [24–27]. Delta-9-tetrahydrocannabinol (THC) is thought to be the main psychotropic agent of the cannabis in the *Cannabis sativa* plant [28]. THC is dose dependently associated to psychiatric symptoms such as psychotic-like experiences in several studies [29]. In contrast, cannabidiol (CBD), a main non-psychoactive component of

* Corresponding author.

** Corresponding author.

E-mail addresses: [hfzj2552@163.com](mailto:hfej2552@163.com) (J. Zhang), ahmupharm@126.com (W. Tang).

¹ X. Jiang and Z.W. Zhang contributed equally to this work.

cannabis, was firstly reported to interfere with the psychomimetic actions of THC in 1974, indicating that CBD may have potential as an antipsychotic agent [30]. CBD can not only antagonize the mental activity caused by THC, but also has wide biological activities, including anxiety, schizophrenia, addiction, neurodegenerative diseases [31]. CBD exhibited neuroprotective effect on iron-induced apoptosis and therapeutic effect in transgenic AD model mouse [32,33], anti-inflammatory and antioxidant effects by inhibiting BACH1 and weakly activating the transcription factor Nrf2 to achieve neuroprotective effects [34]. CBD had the potential to resist the cytotoxicity of $A\beta_{(31-35)}$ and $A\beta_{(25-35)}$ peptides, indicating that CBD can improve AD symptoms by reducing the accumulation of amyloid and the production of amyloid plaques [35]. As shown in Fig. 1, CBD can enter the synaptic cleft and display wide pharmacological effect on some receptors [36,37]. In the synaptic cleft, can CBD bind into ChEs and improve AD by inhibiting ChEs to increase the level of ACh?

Clinical drugs containing amide ($-\text{CONH}-$) and/or carbamate ($-\text{OCONH}-$) motifs can provide privileged structural fragments [38–40]. These motifs are able to interact with a wide range of receptors/enzymes to induce biological responses [41,42]. As a result, there is a growing interest in amide- and carbamate-based scaffolds for medicinal chemists [43,44]. Based on the cholinergic hypothesis, carbamate-like drugs can be regarded as one of the mainstays for the contemporary pharmacotherapy for AD by inhibiting ChEs [45]. Rivastigmine is a pseudo-irreversible inhibitor that forms covalent carbamate adduct with AChE [46]. The molecular docking showed that the carbonyl of the carbamate group tends to form hydrogen bonding interactions, and the N atom is essential for interaction with the ChE binding site.

CBD has sparked wide attention due to its therapeutic potential, and there is considerable interest in synthesizing novel CBD derivatives with improved drug-like properties [47,48]. In this study, using molecular modeling approaches, a series of CBD carbamates

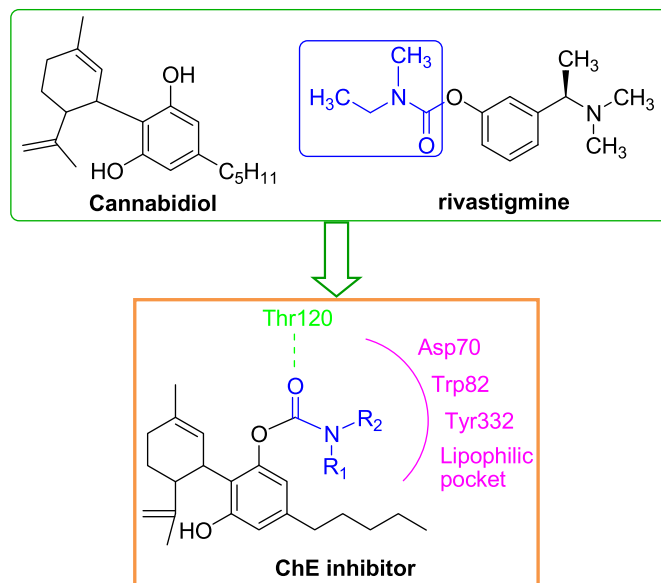


Fig. 2. The general design strategy in this study.

were designed by fragment reassembly followed by docking to predict the bioactivity of the reassembled molecules, followed by *in vitro* and *in vivo* study to identify potent ChE activity (Fig. 2).

2. Results and discussion

2.1. Docking-based structural splicing design

To better explore the capacity of CBD targeting BuChE, we investigated the binding modes by the CDOCKER molecular

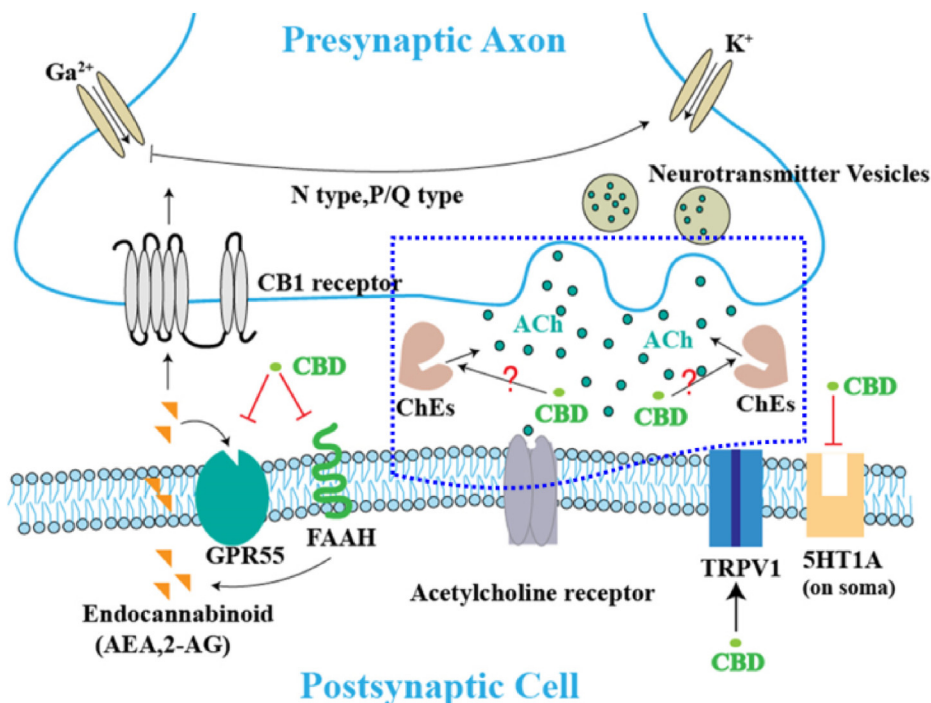


Fig. 1. The relevant pharmacology of CBD in synaptic cells. As a FAAH inhibitor, CBD increases the AEA and 2-AG concentrations to activate retrograde signals. It acts as an agonist at TRPV1 to facilitate cation transport and at the somatic 5HT1A receptor to inhibit adenylate cyclase. It also inhibits AEA through binding to the orphan receptor GPR55 [34,37]. However, can CBD act to ChEs?

docking module in Discovery Studio 2018. CBD could nicely insert into the binding groove of BuChE, forming multiple interactions via π - π interaction interactions between the benzene ring and Trp332, hydrophobic interactions between the cyclohexene ring and Trp82 and His438 and two hydrogen bonds between the hydroxyl and Asp70 and Trp332. The molecular modeling results showed that although both -OH of CBD have modifiable space, only one has a larger space that is suitable to be modified or combined with Thr120 (Fig. 3). Therefore, under the guide of a docking-based structural fragment reassembly approach and the structure characteristics of CBD and rivastigmine, compounds **C1**–**C6** containing single- or double-substituted CBD carbamates were synthesized (Scheme 1).

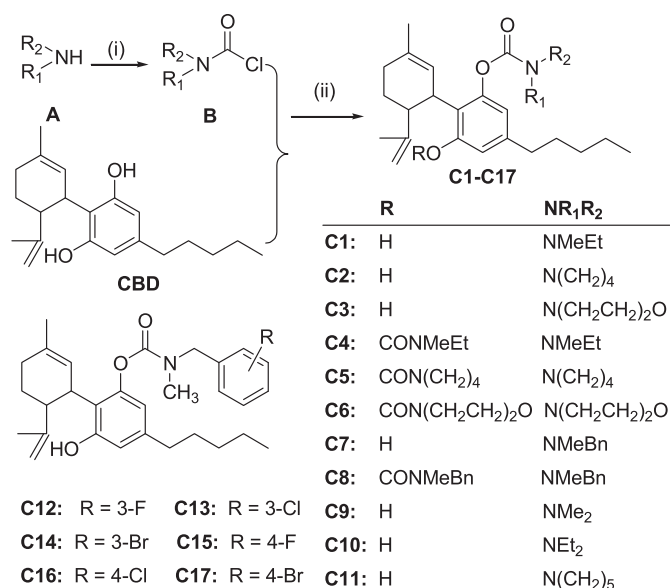
2.2. Inhibition of equine BuChE and electrophorus electricus AChE

Initial screening of CBD carbamates was performed with equine BuChE (*eqBuChE*), *electrophorus electricus* AChE (*eeAChE*), recombinant human AChE (*hAChE*) and BuChE from human serum (*hBuChE*) using modified Ellman's method [49,50].

As shown in Table 1, ChEs inhibition was consistent with the molecular modeling results that one of two hydroxyl groups of CBD is suitable for being modified into a larger space at the active site of *hBuChE*. The *eqBuChE* inhibitory activity of the single-substituted CBD was significantly higher than that of the double-substituted (IC_{50} values for *eqBuChE*, **C1** > **C4**; **C2** > **C5**; **C3** > **C6**; **C7** > **C8**). Compounds with aliphatic amine exhibited better BuChE inhibition than those with cyclic amine (IC_{50} values for *eqBuChE*, **C1**, **C9**, **C10** > **C2**, **C3**; **C4** > **C5**, **C6**), amongst them, compound **C1** with methylethylamine showed similar ChE inhibitory activity to rivastigmine (IC_{50} values for *eeAChE* and *eqBuChE*, 14.95 and 0.077 μ M for **C1**; 16.35 and 0.058 μ M for rivastigmine).

2.3. Optimization and SARs of CBD carbamates

In our recent work, based on the hydrophobic interactions of donepezil at the peripheral anionic site (PAS) of ChE, the introduction of a *tert*-benzylamine significantly improved the BuChE inhibitory activity of the δ -sultone-fused pyrazole scaffold [14,19]. In this work, the *tert*-benzylamine would be introduced into CBD carbamate by the fragment reassembly. As shown in Fig. 4A and B, CBD containing *tert*-benzylamine was well docked into the active site, the benzene ring fell into the hydrophobic pocket through π - π interactions between the benzene ring and Trp82 and Try332, hydrogen bond interaction between the carbonyl of carbamate and Thr120. Under the guide of the molecular modeling, a series of CBD carbamates were designed and synthesized. As shown in Table 1,



Scheme 1. Synthesis of CBD carbamates **C1**–**C17**. Reagents and conditions: (i) triphosgene, NaHCO₃, CH₂Cl₂, -10–0 °C, 6–8 h; (ii) R₁R₂NCOOCl (**C1**–**C17**), 4-DMAP, K₂CO₃, CH₃CN, 60–65 °C.

compounds **C16** and **C17** exhibited nanomolar inhibition on *eqBuChE* (IC_{50} = 5.3 and 7.3 nM, respectively) and >4000 selectivity index for *eqBuChE* over *eeAChE*. Substituted group at benzene ring of *tert*-amine affected *eqBuChE* inhibitory activity, for example, 4-substituted halogen showed better activity than the corresponding 3-substituted (**C15** > **C12**; **C16** > **C13**; **C17** > **C14**). Further, the order of substituted halogen on *eqBuChE* inhibition is Cl \approx Br > F (**C16** \approx **C17** > **C15** for 4-halogen; **C13** \approx **C14** > **C12** for 3-halogen). The structure-activity relationship (SAR) of CBD carbamates was illustrated in Fig. 5.

2.4. Inhibition of hAChE and hBuChE

To determine the potency and selectivity of CBD carbamates for the human enzymes, we tested them for *hBuChE* and *hAChE* inhibitory potential *in vitro*. As shown in Table 2, promising compounds **C1**, **C16** and **C17** showed better *hBuChE* inhibition than rivastigmine (IC_{50} values = 1.51, 1.77 and 2.15 μ M for *hBuChE*, respectively), while they hardly inhibited *hAChE* even at 20 μ M. Hence, compounds **C1**, **C16** and **C17** were found to be highly selective inhibitors of *hBuChE*.

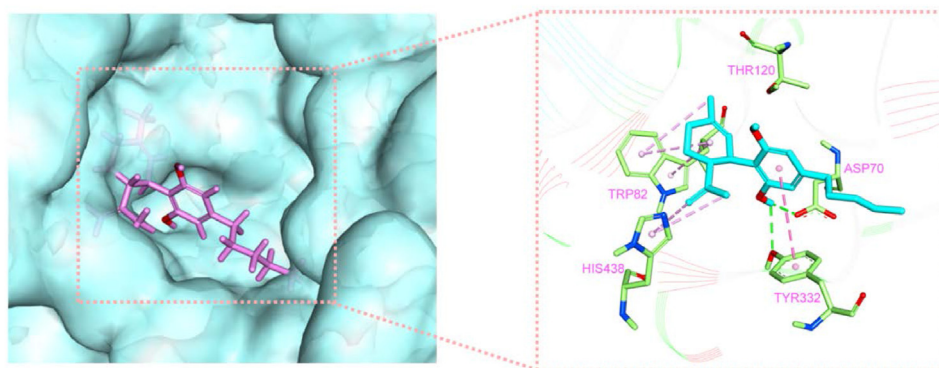


Fig. 3. Binding modes of CBD with *hBuChE* (PDB code: 5LKR). CBD is shown in pink, important residues of the receptor are presented in green. Hydrophobic interactions are shown in pink, hydrogen bonds are shown in green and π - π interactions are shown in dark pink.

Table 1
Chemical Structures of CBD and C1–C17 and Their Inhibitory Activities against *eeAChE* and *eqBuChE*^a.

Compound	IC ₅₀ , μM (or inhibition rate % at 20 μM)		RP of DPPH assay ^d
	<i>eeAChE</i> ^b	<i>eqBuChE</i> ^c	
CBD	17.07 ± 2.43	0.67 ± 0.06	66.7%
C1	14.95 ± 1.02	0.077 ± 0.005	31.1%
C2	na ^e	0.39 ± 0.04	4.9%
C3	na	1.89 ± 0.30	21.1%
C4	na	0.29 ± 0.02	0.1%
C5	na	0.53 ± 0.08	17.8%
C6	na	3.36 ± 0.23	2.0%
C7	na	0.046 ± 0.008	21.1%
C8	na	0.38 ± 0.08	41.8%
C9	36.1 ± 1.8%	0.20 ± 0.01	27.1%
C10	28.4 ± 0.8%	0.37 ± 0.03	40.4%
C11	30.5 ± 5.1%	0.53 ± 0.08	46.8%
C12	na	4.87 ± 0.15	na
C13	na	2.82 ± 0.26	na
C14	na	2.40 ± 0.10	na
C15	na	0.069 ± 0.006	27.0%
C16	21.4 ± 2.8%	0.0053 ± 0.0012	27.1%
C17	na	0.0073 ± 0.0012	41.8%
Donepezil	0.026 ± 0.003	9.24 ± 1.18	1.3%
rivastigmine	16.35 ± 1.54	0.058 ± 0.013	2.5%
ascorbic acid			86.2%

^a Each IC₅₀ value is the mean ± SEM from at least three independent experiments.

^b *eeAChE* from electric eel.

^c *eqBuChE* from horse serum.

^d RP of 1,1-Diphenyl-2-picrylhydrazyl (DPPH) (%) = reduction percentage of DPPH, compounds at a concentration of 100 μM (n = 2).

^e na, no activity.

2.5. DPPH radical scavenging activity assay

1,1-Diphenyl-2-picrylhydrazyl (DPPH) is an extremely effective free radical scavenger that can be used to monitor a chemical reaction that involves free radicals. The DPPH assay was performed with ascorbic acid and donepezil as reference antioxidants to evaluate the ability of the synthesized compounds to scavenge activated oxygen species. As shown in Table 1, almost all compounds exhibited mild free radical scavenging activity with the DPPH RP of 0–46.8% at a concentration of 100 μM, and that of CBD is 66.7%. CBD exhibited close antioxidant activity to vitamin C at a concentration of 100 μM, when OH of CBD was substituted, the activity decreased. The antioxidant activity of CBD carbamates was proportionate to the number of OH. Mono-carbamate of CBD retained almost half antioxidant activity, which may attenuate the

The introduction of carbamate significantly increases activity

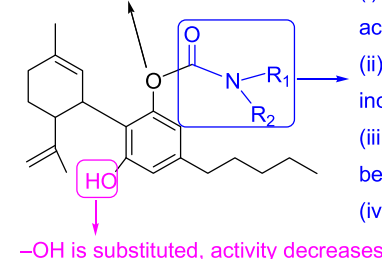


Fig. 5. SARs of the BuChE inhibitor based on compound **C16**.

Table 2
Inhibitory activity on *hAChE* and *hBuChE*^a.

Compound	IC ₅₀ , μM (or inhibition rate % at 20 μM)	
	<i>hAChE</i> ^b	<i>hBuChE</i> ^c
Donepezil	0.018 ± 0.002	11.86 ± 3.51
Rivastigmine	12.2 ± 1.3%	2.71 ± 0.73
C1	13.2 ± 2.9%	1.51 ± 0.48
C16	26.3 ± 3.5%	1.77 ± 0.78
C17	na ^d	2.15 ± 0.77

^a Each IC₅₀ value is the mean ± SEM from at least three independent experiments.

^b *hAChE*.

^c *hBuChE*.

^d na, no activity.

oxidative damage to the cells and tissues caused by the trace of free radicals.

2.6. Kinetic study on the mode of *eqBuChE* inhibition

Rivastigmine, a carbamate drug, was selected as a reference to explore pseudo-irreversible inhibition of CBD carbamates on *eqBuChE*. The mechanism of pseudo-irreversible enzyme inhibition by carbamates can be described by three pivotal steps as shown in Fig. 6 [51,52].

Firstly, the enzyme E forms a reversible enzyme–inhibitor complex (ECX) with the carbamate-based inhibitor CX comparable to reversible competitive inhibitors. This reversible inhibition is quantified by K_d which describes the apparent affinity between the enzyme and the inhibitor in an equilibrium state (Fig. S2). In the second step, the carbamate moiety itself is transferred onto the

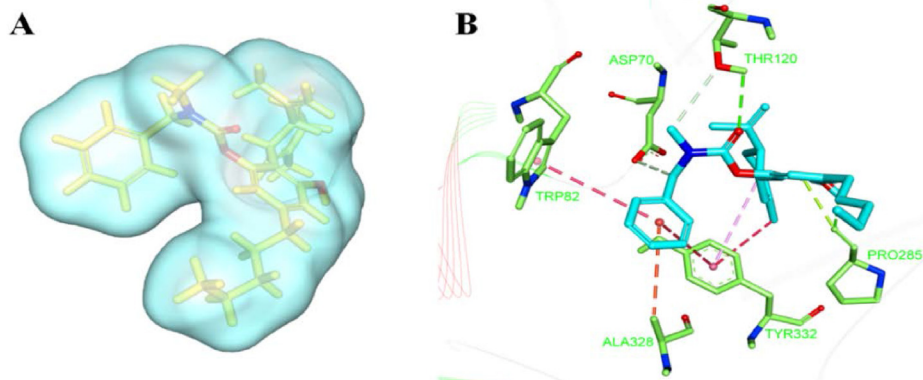


Fig. 4. (A) Alignment of docking mode of **C7** in the receptor. The pocket surface is presented in blue; **C7** is shown in yellow. (B) 3D mode of the interaction of **C7** with receptor *hBuChE*. Hydrophobic interactions are shown in pink, hydrogen bonds are shown in green and π - π interactions are shown in dark pink.

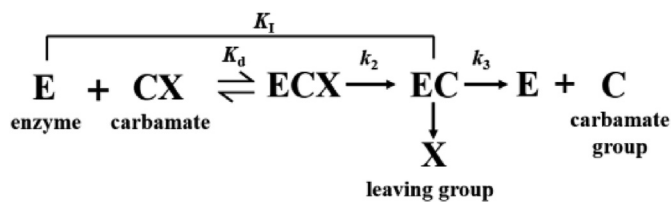


Fig. 6. Pseudo-irreversible inhibition of an enzyme E by carbamates CX.

enzyme with release of the carrier scaffold X, resulting in the carbamoylated enzyme EC. The constant k_2 represents the carbamylation rate of the inhibitor from the reversible complex (ECX) to the carbamoylated enzyme EC. K_1 (k_2/K_d) represents the overall carbamylation rate. The last step is the recovery of the enzyme through slow hydrolysis of EC and release of the carbamate group C with k_3 as the decarbamylation rate constant. Normally, k_3 is significantly lower than k_2 due to the fact that carbamylation occurs much faster than decarbamylation because of the high stability of EC toward hydrolysis [52,53].

As shown in Figs. 7 and S1 and Table 3, compounds **C2** (Fig. 7B) and **C16** (Fig. 7C) inherited the pseudo-irreversible inhibition of BuChE by rivastigmine (Fig. 7A). The kinetics of ChE inhibition by carbamates is strongly influenced by the substituent at the *N*-carbamoyl group, for example, short-chain alkyl carbamates gave relatively rapid carbamylation and decarbamylation, while long-chain alkyl carbamates generally provided a more stable carbamoylated enzyme which is formed slower but also undergoes a slower hydrolysis toward a reactivated enzyme [51]. The carbamylation rate of compound **C2** with short-chain alkyl was significantly higher than that of compound **C16** with long-chain alkyl. The kinetics of enzyme inhibition and reactivation influences the duration of action of a carbamate drug. Therefore, CBD carbamates with high affinity can exert a longer-lasting effect in the body [53,54].

2.7. Further molecular simulation

Halogen-containing phenyl moiety is beneficial for liposolubility and membrane permeability, which can influence the rate of absorption and transport of drugs. As shown in Fig. 8, the molecular docking of compounds **C16** and **C17** showed that the introduction of Cl and Br atoms increases hydrophobic interactions through the p - π interactions with Met437 and Trp430 to further improve BuChE inhibitory activity.

2.8. Molecular dynamics simulation

MD simulation mainly relies on Newtonian mechanics to simulate the motion of a molecular system. This approach can not only obtain the trajectory of atoms but also enables the observation of various microscopic details during atomic motion [55,56].

Table 3

Kinetic values for carbamylation and decarbamylation on eqBuChE for selected compounds.

Compound	K_d^a (μM)	k_2^b (min^{-1})	K_1^c ($\mu\text{M}^{-1} \text{min}^{-1}$)	k_3^d (min^{-1}) $\times 10^3$
C2	0.35 ± 0.04^e	0.33 ± 0.04	0.94 ± 0.03	5.13 ± 0.57
C16	0.013 ± 0.001	0.26 ± 0.01	20.26 ± 2.75	5.20 ± 0.56
rivastigmine	1.15 ± 0.09	0.30 ± 0.03	0.26 ± 0.04	4.97 ± 0.59

^a The apparent affinity between the enzyme and the inhibitor in an equilibrium state.

^b The carbamylation rate.

^c The overall carbamylation rate.

^d The decarbamylation rate.

^e Each value is the mean \pm SEM from at least three independent experiments.

Compound **C16** was docked into the hBuChE pocket and then subjected to MD simulation to examine the structural stability of simulation system. MD simulation of complexes was performed for 100 ns period. In this study, the kinetic energy of compound **C16** started to increase by temperature and time until a steady state was reached. As shown in Fig. 9A, before 60,000 ps, the entire system of the complex hBuChE-**C16** was in a stable state. After 60,000 ps, an obvious upward trend was emerged, especially at 70,000 ps, after which the overall system was relatively stable, and the wave range of RMSD was within 1 Å. Subsequently, calculated by the MM-PB(GB)SA method (Fig. 9B), the total binding free energy was -41.09 kcal/mol for the complex of hBuChE-**C16**, and the van der Waals energy was -56.14 kcal/mol. Fig. 9C was the contributions of hot residues in the binding pocket of hBuChE. Under normal circumstances, a residue with lower interaction energy than -1 kcal/mol was considered to be essential for ligand recognition and combination. As disclosed in docking studies, π - π interactions between **C16** and Trp82 (-1.71 kcal/mol) and Tyr332 (-2.35 kcal/mol), hydrogen bonding of **C16** with Thr120 (-1.35 kcal/mol), and π -alkyl interactions of **C16** with Met437 (-3.98 kcal/mol) and His438 (-1.14 kcal/mol) were significant for binding to hBuChE.

2.9. In vitro cytotoxicity evaluation

To examine the cytotoxicity of the CBD and its carbamates, the effects of CBD and **C16** on cell viability were determined at 6.25, 12.5, 25 and 50 μM in parallel with donepezil in human hepatoblastoma HepG2 cells and human normal liver cells L02 [57]. As shown in Fig. 10A, exposing HepG2 cells for 24 h to **C16** and donepezil at either 12.5 μM or 25 μM did not significantly reduce cell viability. However, at 50 μM , both **C16** and donepezil slightly affected viability, and the cytotoxic effect was almost same for **C16** and donepezil (88.3% vs 91.1%); while CBD at 25 μM significantly affected viability ($p < 0.01$), and the cell viability decreased to 20.1%. Fig. 10B showed that after exposing L02 cells for 24 h to CBD, **C16** and donepezil the similar trend was observed. Up to 50 μM , both **C16** and donepezil slightly affected viability, and the cytotoxic effect was 96.0% and 92.6%; while CBD at 50 μM significantly affected viability ($p < 0.01$), and the cell viability decreased to 44.9%. The results showed that **C16** is less toxic to HepG2 and L02 cells than CBD. All in all, the cell toxicity profile of **C16** roughly matched that of donepezil, much lower than that of CBD. CBD may be cytotoxicity-related antioxidant activity, while **C16** reduced the activity by half, therefore, **C16** could be the best candidate for further investigation.

2.10. Oil/water partition coefficient

The log P (o/w) (octanol-water partition coefficient) can reflect the absorption of a drug in an organism and the optimum value was around 2.0 ± 0.7 for the central nervous system penetration [58,59].

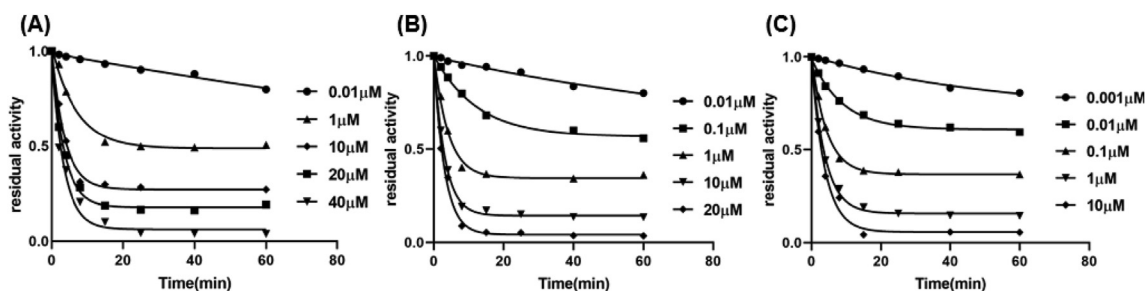


Fig. 7. Time- and concentration-dependent carbamylation of *eg*BuChE by rivastigmine (A), C2 (B) and C16 (C). Residual activity indicates the percentage of remaining enzyme activity that has not been carbamylated (n = 3).

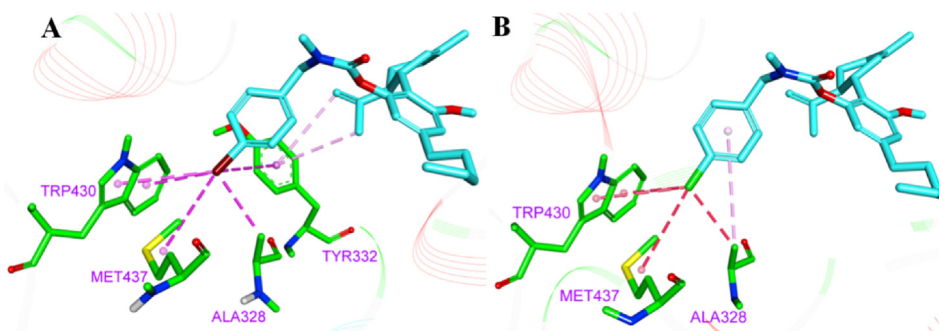


Fig. 8. 3D mode of interactions of C16 (A) and C17 (B) with receptor *h*BuChE. Cl and Br atoms are presented by bright green and dark brown respectively; p-π interactions are shown in dark pink; important residues are presented in purple.

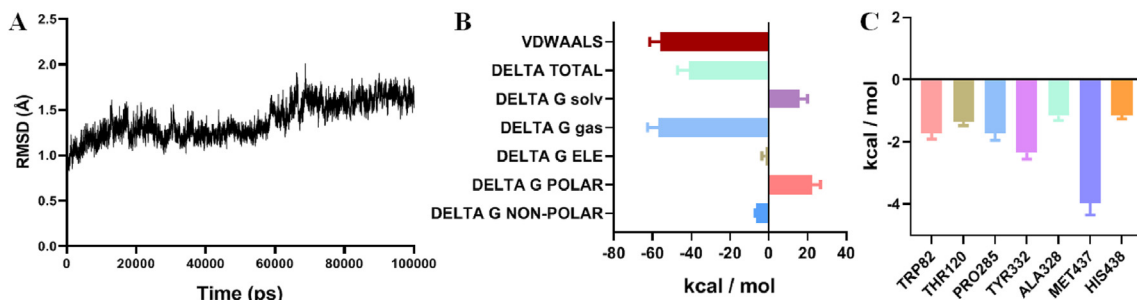


Fig. 9. (A) The RMSD plots of complexes vs time; (B) Total binding free energy and its component; (C) Residue contribution for receptor-ligand combination.

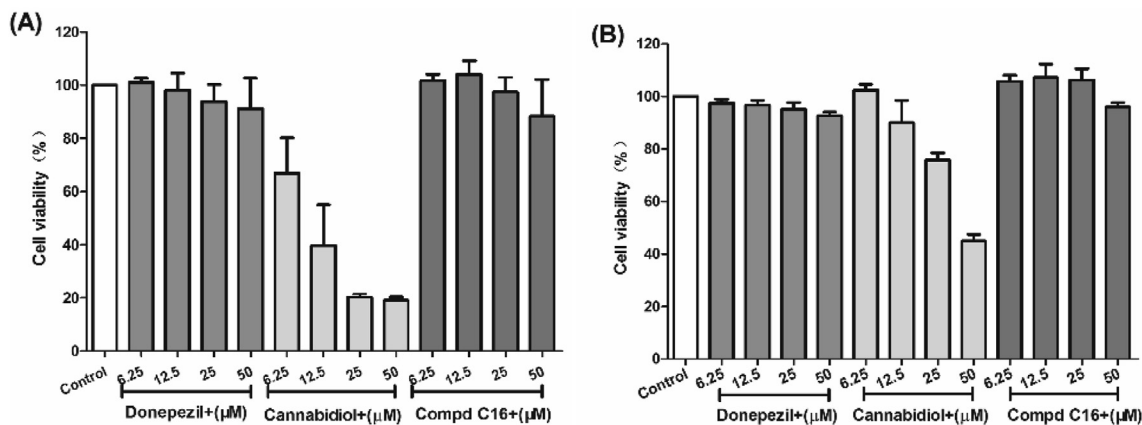


Fig. 10. Cytotoxicity of CBD, C16 and donepezil was tested at concentrations in the range 0–50 μM in HepG2 (A) cells and L02 (B) cells for 24 h. Untreated cells were used as control. Results are expressed as percentage of cell survival vs untreated cell (control) and shown as mean ± SD (n = 3).

Therefore, log *P* values of active compounds were usually used to predict the ability to cross blood-brain barrier (BBB). As shown in Table 4, log *P* values of active compounds ranged from 1.6 to 2.6, which implied that the modified CBDs have proper lipophilicity to cross BBB.

2.11. BBB permeability study

The central nervous system (CNS) is the ultimate therapeutic target of the anti-AD agent, it is essential to evaluate the BBB penetration capacity of the synthesized compounds in the drug discovery process [18,58]. Hence, BBB penetrating ability of CBD, **C1** and **C16** was estimated using a parallel artificial membrane permeation assay (PAMPA) BBB model. To validate the experimental procedure, six commercial drugs with reported values were chosen. A plot of experimental versus bibliographic data presented a good linear correlation, $P_e(\text{exp.}) = 0.9219 P_e(\text{bibl.}) - 0.4558$ ($R^2 = 0.9696$) (Fig. 11B). CBD, **C1** and **C16** were tested following this procedure, and the results in Fig. 11A showed that permeability values of tested compounds are above 4×10^{-6} cm/s. CBD, **C1** and **C16** were indicated to be capable of BBB penetration.

2.12. Neuroprotective study

The protective effects of CBD and **C16** against free radicals damage were assessed by measuring their ability against H₂O₂-induced injury according to the reported protocol [18,19]. After exposing PC12 cells to 100 μM H₂O₂, cell viability obviously decreased to 38.7% ($p < 0.01$ vs control), manifesting high sensitivity to H₂O₂-induced injury. As shown in Fig. 12, **C16** had weak protective effect in a dose-dependent manner against H₂O₂-induced PC12 cell injury. At a concentration of 25 μM, **C16** exhibited significant neuroprotective effect with cell viability of 41.9% and was stronger than CBD with that of 17.9%, which clarified that **C16** could efficiently capture the hydroxyl radical generated by H₂O₂.

2.13. In vivo acute toxicity evaluation

In vivo safety was carried out by a single-dose acute toxicity evaluation in ICR mice. After intragastric administration of **C16** at a dose of 1.0 g/kg, no death and abnormal behaviors were observed. Moreover, the body weights of all mice in vehicle and test groups were recorded and shown in Fig. 13. Within the 14 days after a single-dose administration, the body weights gradually enhanced (Fig. 13A), and the mean body weight of the mice in test group presented no significant differences as those in vehicle group. Hence, **C16** could be well tolerated *in vivo* at a high dose of 1.0 g/kg.

Additionally, the *in vivo* hepatotoxicity of **C16** was evaluated by levels of aspartate aminotransferase (AST) and alanine aminotransferase (ALT) (Fig. 13B) and hematoxylin-eosin (HE) staining images (Fig. 13C). Heparinized serum was collected 8, 22, and 36 h after the intragastric administration of the vehicle and **C16** (30 mg/kg), and no significant differences in two biomarkers were

observed at all time points between vehicle and **C16** groups. Paraffin sections were observed 36 h after administration of the vehicle (control group) or **C16** (30 mg/kg). Neither pericentral necrosis nor distinct fatty degeneration of the hepatocytes of the surrounding intermediate and periportal zones was discovered in immunohistochemical staining images (Fig. 13D). Therefore, obvious acute hepatotoxicity triggered by treatment of **C16** was observed. Taken together, **C16** exhibited high *in vivo* safety, ensuring its further pharmacology development.

2.14. In vivo behavioral studies

Cognition-improving potency is of utmost importance for anti-AD agents. Scopolamine is a nonselective muscarinic ACh receptor antagonist, and it produces cognitive deficits in test subjects that are comparable to those caused by the cholinergic deficit characteristic of AD. ChE inhibitors alleviate this cognitive deficits by increasing the levels of synaptic ACh (notably in the brain), which results in displacement of scopolamine from muscarinic ACh receptors. The Morris water maze (MWM) task is a hippocampal-dependent memory and spatial learning task that is mainly used to study the effect on long-term memory by reducing the time to reach the escape platform (ie, the escape time latency). *In vitro* ChE inhibitory activity must translate into behavioral effects and improve the cognition *in vivo* [18,60,61]. Scopolamine was used to induce cognitive deficits in test animals (1 mg/kg; intraperitoneal (ip) injection prior to the acquisition trials in each test). MWM test was used to study the ameliorating potential of **C16** against scopolamine-induced cognition impairment in mice. The results demonstrated impairment in learning and memory by a model group of animals with a significant prolongation of ELT. The administration of **C16** and donepezil exhibited a remarkable reduction in ELT (Fig. 14A) and significantly improved the overall target quadrant preference (the number to cross the platform and the swimming time in the target quadrant) compared to model group (Fig. 14B and C). The results signified that **C16** had effect in ameliorating cognitive dysfunction, which may be attributed to superior activity.

In order to give more detailed information about the anti-AD profile of **C16**, we conducted an Aβ₁₋₄₂ (intracerebroventricular (icv) injection)-induced cognition-impaired model [18,62,63]. AD-like cognitive dysfunction was caused by icv injection of the oligomerized Aβ₁₋₄₂ peptide (10 μg per mouse) on day 1 (Fig. 15A). Meanwhile, mice icv injected with saline (same volume) were set as a sham-operation group. Donepezil (positive control) and **C16** were administered (po) from days 3–14. Behavioral studies were carried out by MWM. The water maze study included 5 days of learning and memory training (on days 10–14) and a probe trial on the sixth day (on day 15). As shown in Fig. 15B–E, icv saline did not affect the cognitive and learning capacity, with no differences from the blank control group in regard to undifferentiated alternation performance, latency to target, and trajectory confusion. Treatment with donepezil (15 mg/kg) could significantly shorten the latency, simplified the trajectories to the platform, and improved the alternation performance. Moreover, administration with **C16** (5 mg/kg) or donepezil (15 mg/kg) could obviously prevent the impact of Aβ₁₋₄₂ peptide icv injection and almost entirely recover the cognitive function to the normal level. Furthermore, **C16** exhibited better efficacy than the donepezil in the MWM test, reduced target latency (Time: **C16** < donepezil < model group), and much simplified trajectory to the target. As shown in Fig. 15F, compared to the control or sham-operation groups, the total level of the Aβ₁₋₄₂ peptide in the icv Aβ₁₋₄₂ group was significantly enhanced, indicating a successful modeling. Furthermore, mice treated with donepezil or **C16** presented obvious reduction of the Aβ₁₋₄₂ peptide

Table 4
Log *P* values of active compounds.

Compound	Log <i>P</i> ^a
CBD	1.67
C1	1.92
C4	2.57
C7	2.20
C16	2.38
C17	2.37

^a Octanol–water partition coefficients were measured by the shake flask method.

Commercial drug	$P_e \times 10^{-6}$ cm/s		BBB permeation ^c
	Bibl. ^a value	Exp. ^b value	
Hydrocortisone	1.9	1.71	CNS -
Testosterone	17	15.6	CNS +
Ofloxacin	0.8	1.05	CNS -
Clonidine	5.3	7.2	CNS +
Piroxicam	2.5	1.79	CNS -
Progesterone	9.3	9.31	CNS +
CBD	--	22.66	CNS +
C1	--	18.81	CNS +
C16	--	12.9	CNS +

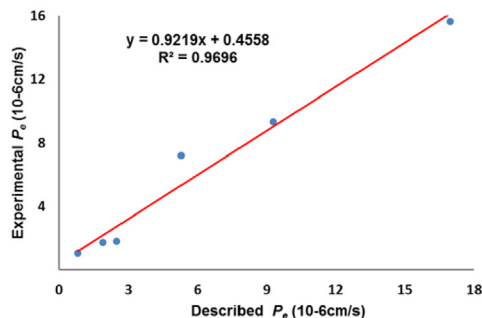


Fig. 11. PAMPA-BBB penetration study of CBD, **C1** and **C16**. (A) Results of the PAMPA-BBB assay for six commercial drugs used in the experimental procedure validation and CBD, **C1** and **C16**. ^a Bibl. values are reported data from the reference; ^b All tests were obtained from three independent experiments; ^c “CNS +” (high BBB permeation): $P_e (\times 10^{-6} \text{ cm/s}) > 4.0$; “CNS +/-” (uncertain BBB permeation): $P_e (\times 10^{-6} \text{ cm/s})$ from 2.0 to 4.0; “CNS -” (low BBB permeation): $P_e (\times 10^{-6} \text{ cm/s}) < 2.0$. (B) Linear correlation presenting experimental versus bibliographic data of commercial drugs. $P_e (\text{exp.}) = 0.9219 P_e (\text{bibl.}) - 0.4558$ ($R^2 = 0.9696$).

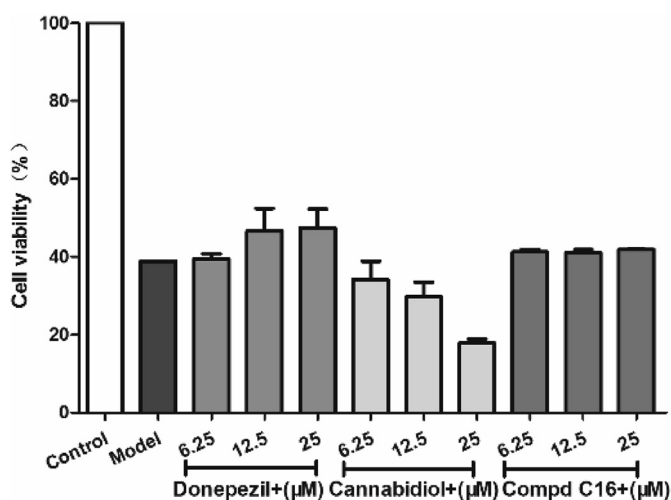


Fig. 12. Neuroprotective effect of CBD and **C16** (0–25 μM) against H_2O_2 -induced (100 μM) PC12 neurons injury for 24 h (cells are given the CBD or **C16** and incubated for 3 h and then given H_2O_2 peroxide to model). Results represent mean \pm SEM ($n = 3$).

(19.0% or 31.6%, respectively). Meanwhile, staining of the hippocampus in Fig. 15G showed that β -amyloid plaque was obvious in the hippocampus of model group compared to control group. The result is consistent with the behavioral test conclusion, supporting that **C16** could effectively improve the cognitive function of AD mice by decreasing the BuChE level and its further neuroprotective effects against $\text{A}\beta$ toxicity. Additionally, none of the treatments (icv saline or peptide or po compound) influenced the mice body weight during therapy period, showing a good safety of **C16** (Fig. 15H).

2.15. Histopathology in hippocampal CA1 and CA3 regions

Hippocampus is one of the most important parts for spatial learning and memory, especial for CA3 to CA1 loop [64–67]. To further study the effect of active compound **C16** against the $\text{A}\beta_{1-42}$ -induced cognitive impairment, the intact brains of the test mice were collected from the behavioral experiment on the last day to observe the histopathology of hippocampus CA1 and CA3 regions. The morphology of pyramidal neurons was assessed by H&E staining. The number of normal cells in hippocampal CA1 and CA3 regions were counted. Each pyramidal neuron was identified by its shape, size, position and visible nucleus. As shown in Fig. 16A, neuronal density was reduced in $\text{A}\beta_{1-42}$ -induced model mice with

numerous scattered shrinking neurons and nuclear pyknosis in hippocampal CA1 and CA3 regions. The quantitative analysis showed that the increase of neuronal density was prominent at hippocampal and especially at the CA1 region in **C16**-treatment group, compared to the control group (Fig. 16B and C).

3. Conclusions

This study demonstrated the effectiveness of using a docking-based structural splicing and reassembly strategy to discover potent and selective BuChE inhibitors. Based on the structure characteristics of marketed drugs CBD and rivastigmine, a series of CBD carbamates were synthesized. Subsequently, *in vitro* ChEs assay revealed that BuChE inhibition of single-substituted CBD was superior to that of the double-substituted. In view of the structure of donepezil, the introduction of a *tert*-benzylamine significantly increased the activity. All synthesized compounds showed selective BuChE inhibitory activity, amongst them, compounds **C16** and **C17** exhibited high inhibition on BuChE (*ee*AChE $\text{IC}_{50} > 20 \mu\text{M}$, *eq*BuChE $\text{IC}_{50} = 5.3$ and 7.3 nM , respectively; *h*AChE $\text{IC}_{50} > 20 \mu\text{M}$, *h*BuChE $\text{IC}_{50} = 1.77$ and $2.15 \mu\text{M}$, respectively) and >4000 -fold selectivity for BuChE over AChE. The enzymic kinetics study revealed that **C16** was a pseudo-irreversible BuChE inhibitor ($K_d = 13 \text{ nM}$, $k_2 = 0.26 \text{ min}^{-1}$). Compared to CBD, **C16** almost decreased the antioxidant capacity by half. The molecular docking and dynamics proved that **C16** was well fallen into the active pocket of BuChE and formed diverse interactions with the key residues around the pocket. **C16** also exhibited benign BBB penetrating ability. The results of *in vitro* and *in vivo* safety showed that **C16** possessed good neural and hepatic safety and was tolerated up to a dose of 1.0 g/kg. In the subsequent *in vivo* behavioral study, **C16** remarkably reduced the scopolamine-induced cognitive impairment in the mice model. In the $\text{A}\beta_{1-42}$ -induced cognition-impairment study, treatment with **C16** significantly prevented the impact of $\text{A}\beta_{1-42}$ toxicity and almost entirely recovered the cognitive function to the normal level. Moreover, the evaluation of the $\text{A}\beta_{1-42}$ total amount confirmed its anti-amyloidogenic profile. However, as a selective BuChE inhibitor, **C16** can produce remarkable cognitive improving and anti-amyloidogenic effects. Hence, **C16** had significant potentiality to be further developed as promising therapeutics for AD treatment.

4. Experimental section

4.1. General methods of chemistry

All chemicals, reagents and solvents were purchased from

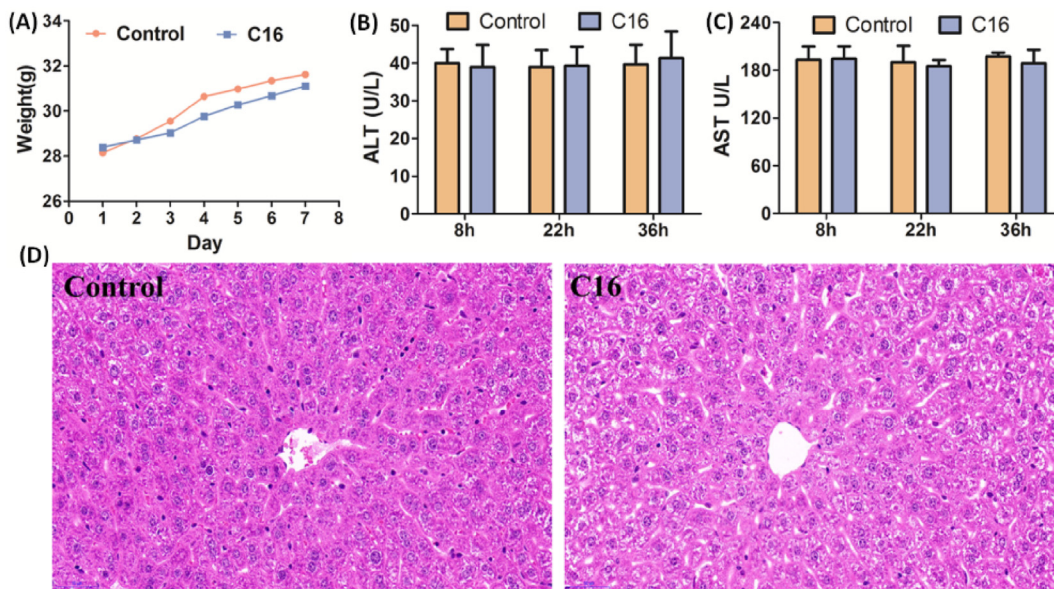


Fig. 13. Results of in vivo acute toxicity evaluation. (A) Body weight of ICR mice (g)-time points of measurement (day). (B) ALT and AST activities at 8, 22, and 36 h after the administration of the vehicle only (control) or **C16**. (C) Histomorphological appearance of mice livers after treatment with control or **C16**. Results represent mean \pm SEM (n = 10), HE staining's view is 50 μ m.

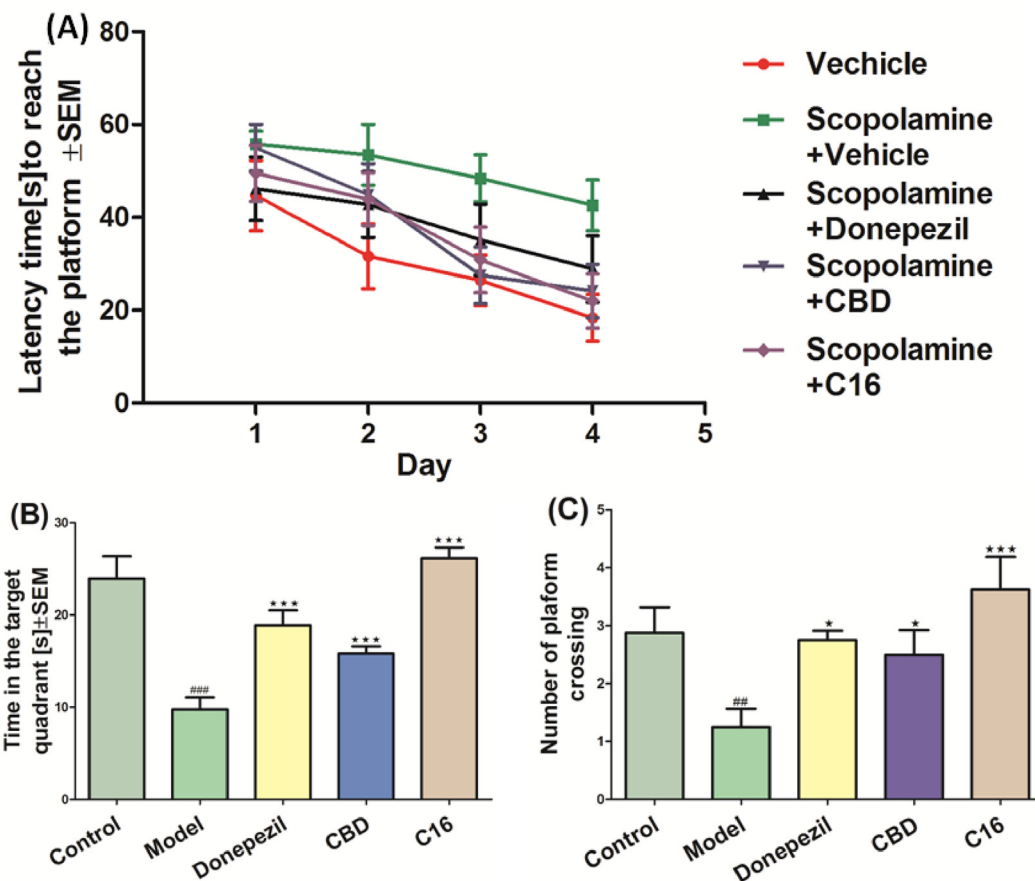


Fig. 14. Effects of **C16**, CBD and donepezil on scopolamine-induced memory impairment in the MWM task. (A) Learning curves of the escape latencies for Control (vehicle-treated mice, red), Model (scopolamine-treated control mice, green), CBD (blue), **C16** (purple) and donepezil (black) (scopolamine-induced memory-impaired mice treated with 20 mg/kg CBD, 20 mg/kg **C16** and 10 mg/kg donepezil, respectively) during the acquisition phase; (B) Time to swim in the target quadrant the acquisition phase in Control, Model, CBD, and **C16** or donepezil; (C) The number to cross the platform during the acquisition phase in Control, Model, CBD, and **C16** or donepezil. Data are means \pm SEM (n = 8). Statistical analysis: repeated-measures ANOVA, followed by Bonferroni posthoc comparisons. $^{##}p < 0.01$, $^{###}p < 0.001$ (vs control group), $^{*}p < 0.05$, $^{***}p < 0.001$ (vs scopolamine + vehicle-treated mice).

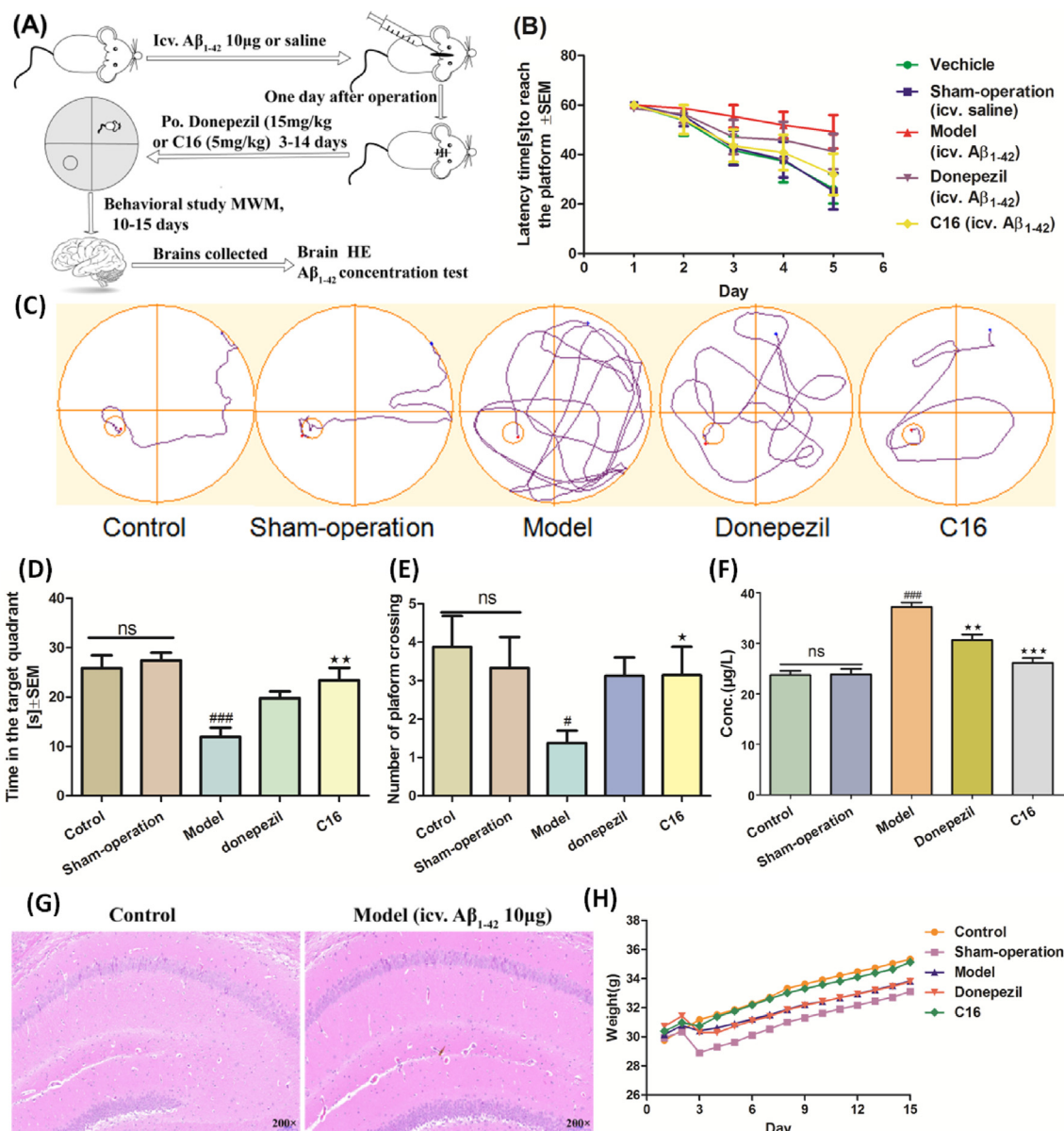


Fig. 15. Effects of **C16** and donepezil on the oligomerized $A\beta_{1-42}$ -induced impairment experiment in the MWM task. (A) Protocol followed for the in vivo experiment. Abbreviations: icv, intracerebroventricular injection; po, orally administration; MWM, morris water maze; HE, hematoxylin-esin. (B) Learning curves of the escape latencies for vehicle-treated mice, sham-operation (icv. saline) mice, model (icv. $A\beta_{1-42}$ 10 μ g) mice and mice treated with 5 mg/kg **C16** or 15 mg/kg donepezil during the acquisition phase. (C) Average tracks of mice in the MWM on the last day of study. (D) Time to swim in the target quadrant the acquisition phase in control (vehicle-treated mice), sham-operation, model, **C16** or donepezil. (E) The number to cross the platform during the acquisition phase in control, sham-operation, model, **C16** or donepezil. (F) $A\beta_{1-42}$ total amount in mice brains of different groups. The $A\beta_{1-42}$ total amount was quantified by using a mouse $A\beta_{1-42}$ ELISA kit. (G) Histomorphological appearance of mice brains after treatment with the vehicle (control) or model (icv. $A\beta_{1-42}$ 10 μ g). HE staining's view is 100 μ m. (H) Daily weight of mice in different groups during the therapy period. Data are presented as means \pm SEM ($n = 8$; # $p < 0.05$, ### $p < 0.001$ vs control group; * $p < 0.05$, ** $p < 0.01$, *** $p < 0.001$ vs $A\beta_{1-42}$ peptide model group).

commercial sources and used without further purification. Reactions were checked by thin-layer chromatography (TLC) on pre-coated silica gel plates (Qingdao Marine Chemical Factory, GF254); spots were visualized by UV at 254 nm. Melting points are determined on a XT4MP apparatus (Taik Corp., Beijing, China) and are not corrected. The purity (relative content) of active compounds was determined by HPLC through area normalization method. ^1H NMR and ^{13}C NMR spectra were recorded on Bruker AV-400 or AV-600 MHz instruments using CDCl_3 and $\text{C}_6\text{D}_5\text{N}$ as solvent. Chemical shifts are reported in parts per million (δ) downfield from the signal of tetramethylsilane (TMS) as internal standards. Coupling constants are reported in Hz. The multiplicity is defined by s (singlet),

d (doublet), t (triplet), or m (multiplet). High resolution mass spectra (HRMS) were obtained on an Agilent 1260–6221 TOF mass spectrometry.

4.2. General synthetic information of target compounds

4.2.1. General synthetic information of carbamyl chlorides (B)

A solution of the secondary amine (A) (30.0 mmol) in CH_2Cl_2 (5 mL) was added dropwise, over half of an hour, to a stirred slurry of sodium bicarbonate (5.04 g, 60 mmol) and triphosgene (5.94 g, 20 mmol) in dichloromethane (30 mL) at -10°C . The reaction mixture was left to warm to room temperature and stirred for

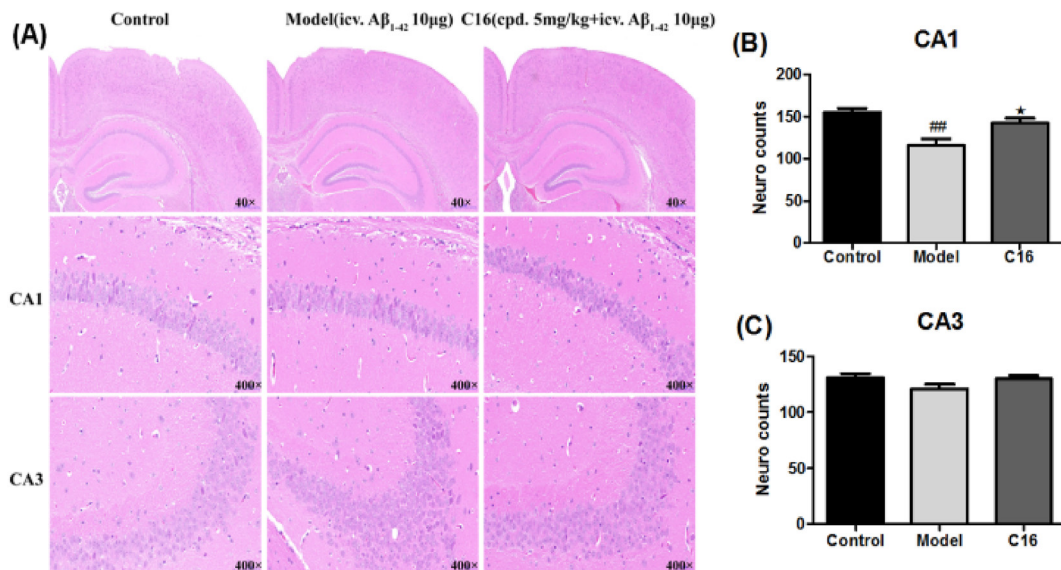


Fig. 16. (A) Morphology in hippocampal CA1 and CA3 regions using hematoxylin-eosin-staining. Scale bar in Hippocampus positioning = 500 μm, scale bar in CA1 and CA3 regions = 50 μm; (B) Neuron counts in CA1 region; (C) Neuron counts in CA3 region. Data were expressed as the mean ± S.E.M. (N = 3). ###*p* < 0.01 vs control group; **p* < 0.05 vs Aβ₁₋₄₂ peptide model group.

6–8 h. The mixture was then filtered and the filtrate was evaporated under reduced pressure to give the carbamyl chloride crude product. The crude product was distilled under reduced pressure or purified by chromatography on silica, with petroleum ether–CH₂Cl₂ as mobile phase, to give the desired product (**B**).

4.2.2. General synthetic information of CBD carbamate derivatives (C1–C17)

Carbamyl chloride **B** (1 equiv. or 1.5 equiv.) was added to a mixture of anhydrous K₂CO₃ (2 equiv.), 4-DMAP (0.2 equiv.), and CBD (0.50 mmol) in 5 mL MeCN. The reaction mixture was warmed to 60–65 °C and stirred for 5–10 h under an argon atmosphere. The reaction was monitored by TLC. On completion of the reaction the solvent was evaporated under reduced pressure. Water (20 mL) was added to the residue and the mixture was extracted with CH₂Cl₂ (2 × 30 mL). The combined organic phases were washed sequentially with 5% NaOH solution (20 mL), 5% HCl solution (20 mL), and saturated aqueous sodium chloride (25 mL), dried over anhydrous Na₂SO₄, and filtered. The solvent was evaporated under reduced pressure and the residue was purified by silica gel flash column chromatography (mobile phase 2:1 CH₂Cl₂–EtOAc) to give compounds **C1–C17**.

4.2.3. 6-Hydroxy-5'-methyl-4-pentyl-2'-(prop-1-en-2-yl)-1',2',3',4'-tetrahydro-[1,1'-biphenyl]-2-yl ethyl(methyl)carbamate (C1)

Light yellow oil, yield 36%; purity, 96.0%. ¹H NMR (400 MHz, CDCl₃) δ 6.52 (s, 1H), 6.43 (d, *J* = 11.7 Hz, 1H), 5.59 (s, 1H), 4.55 (d, *J* = 56.4 Hz, 2H), 3.57 (s, 1H), 3.04–2.95 (m, 3H), 2.47 (dd, *J* = 15.0, 7.1 Hz, 3H), 1.81–1.54 (m, 12H), 1.38–1.12 (m, 10H), 0.87 (t, *J* = 6.9 Hz, 3H). ¹³C NMR (101 MHz, CDCl₃) δ 155.5, 154.6, 154.3, 149.9, 142.6, 139.9, 123.7, 119.7, 114.5, 114.1, 110.9, 44.0, 43.8, 38.0, 37.9, 35.4, 34.1, 33.7, 31.6, 30.6, 23.6, 22.5, 20.4, 14.1, 12.9. HRMS (ESI) *m/z* [M + Na]⁺: 422.2661, calcd for C₂₅H₃₇NNaO₃: 422.2665.

4.2.4. 6-Hydroxy-5'-methyl-4-pentyl-2'-(prop-1-en-2-yl)-1',2',3',4'-tetrahydro-[1,1'-biphenyl]-2-yl pyrrolidine-1-carboxylate (C2)

Light yellow oil, yield 43%; purity, 98.4%. ¹H NMR (400 MHz,

CDCl₃) δ 6.54 (s, 1H), 6.49 (d, *J* = 1.6 Hz, 1H), 6.05 (s, 1H), 5.62 (s, 1H), 4.56 (d, *J* = 51.8 Hz, 2H), 3.61 (d, *J* = 36.4 Hz, 1H), 3.60–3.41 (m, 4H), 2.54–2.48 (m, 2H), 2.13 (dd, *J* = 37.3, 16.7 Hz, 2H), 1.98–1.89 (m, 4H), 1.85–1.69 (m, 5H), 1.64–1.57 (m, 4H), 1.37–1.24 (m, 6H), 0.89 (t, *J* = 6.9 Hz, 3H). ¹³C NMR (101 MHz, C₆D₅N) δ 158.1, 153.9, 152.4, 149.7, 142.1, 131.7, 127.4, 122.9, 116.3, 113.5, 111.6, 47.3 (2C), 46.9, 36.1, 32.1, 31.6, 31.4, 30.3, 26.6, 25.6 (2C), 24.0, 23.2, 20.0, 14.6. HRMS (ESI) *m/z* [M + H]⁺: 412.2846, calcd for C₂₆H₃₈NO₃: 412.2846.

4.2.5. 6-Hydroxy-5'-methyl-4-pentyl-2'-(prop-1-en-2-yl)-1',2',3',4'-tetrahydro-[1,1'-biphenyl]-2-yl morpholine-4-carboxylate (C3)

Light yellow oil, yield 36%; purity, 97.5%. ¹H NMR (400 MHz, CDCl₃) δ 6.61–6.38 (m, 2H), 6.08 (s, 1H), 5.57 (s, 1H), 4.54 (d, *J* = 58.5 Hz, 2H), 3.77–3.46 (m, 8H), 2.61–2.38 (m, 3H), 2.27–1.96 (m, 2H), 1.92–1.48 (m, 11H), 1.35–1.26 (m, 4H), 0.87 (t, *J* = 6.9 Hz, 3H). ¹³C NMR (101 MHz, C₆D₅N) δ 158.1, 154.6, 152.3, 149.5, 142.2, 131.9, 127.3, 122.8, 115.9, 113.6, 111.7, 67.3 (2C), 45.8, 44.9 (2C), 36.1, 32.1, 31.5, 31.4, 30.3, 24.1, 23.2, 20.0, 14.6. HRMS (ESI) *m/z* [M + Na]⁺: 450.2611, calcd for C₂₆H₃₇NNaO₄: 450.2614.

4.2.6. 5'-methyl-4-pentyl-2'-(prop-1-en-2-yl)-1',2',3',4'-tetrahydro-[1,1'-biphenyl]-2,6-diyl bis(ethyl(methyl)carbamate) (C4)

Light white oil, yield 39%; purity, 95.6%. ¹H NMR (400 MHz, CDCl₃) δ 6.76 (s, 1H), 6.71 (d, *J* = 9.5 Hz, 1H), 5.38 (d, *J* = 8.6 Hz, 1H), 4.54 (d, *J* = 18.2 Hz, 2H), 3.66–3.37 (m, 6H), 2.99 (d, *J* = 21.8 Hz, 3H), 2.66–2.48 (m, 3H), 2.11–1.71 (m, 8H), 1.66–1.45 (m, 8H), 1.37–1.10 (m, 8H), 0.87 (t, *J* = 6.2 Hz, 3H). ¹³C NMR (101 MHz, CDCl₃) δ 155.0 (2C), 150.4 (2C), 148.1, 141.9, 137.4 (2C), 137.3, 128.9 (2C), 128.8 (2C), 128.3 (4C), 127.8 (2C), 127.5, 126.7, 125.4 (2C), 111.1, 53.0, 52.8, 46.0, 38.8, 35.5, 34.9, 34.0, 31.9, 30.8, 30.7, 29.2, 23.5, 22.7, 20.3, 14.3. HRMS (ESI) *m/z* [M + Na]⁺: 507.3185, calcd for C₂₉H₄₄N₂NaO₄: 507.3193.

4.2.7. 5'-methyl-4-pentyl-2'-(prop-1-en-2-yl)-1',2',3',4'-tetrahydro-[1,1'-biphenyl]-2,6-diyl bis(pyrrolidine-1-carboxylate) (C5)

White oil, yield 44%; purity, 99.0%. ¹H NMR (400 MHz, CDCl₃)

δ 6.76 (s, 2H), 5.39 (s, 1H), 4.53 (d, $J = 20.4$ Hz, 2H), 3.65 (d, $J = 12.4$ Hz, 1H), 3.45 (m, 8H), 2.58 (m, 3H), 2.04 (s, 2H), 1.93 (dt, $J = 13.3, 5.9$ Hz, 8H), 1.82–1.69 (m, 2H), 1.65–1.45 (m, 8H), 1.36–1.23 (m, 4H), 0.87 (t, $J = 6.9$ Hz, 3H). ^{13}C NMR (101 MHz, CDCl_3) δ 152.9 (2C), 150.0 (2C), 147.9, 141.5, 131.6, 126.4 (2C), 125.4 (2C), 110.8, 46.4 (2C), 46.2 (2C), 46.0, 38.4, 35.3, 31.6, 30.8, 30.5, 28.9, 25.9 (2C), 24.9 (2C), 23.2, 22.5, 19.9, 14.1. HRMS (ESI) m/z $[\text{M} + \text{Na}]^+$: 531.3186, calcd for $\text{C}_{31}\text{H}_{44}\text{N}_2\text{NaO}_4$: 531.3193.

4.2.8. 5'-methyl-4-pentyl-2'-(prop-1-en-2-yl)-1',2',3',4'-tetrahydro-[1,1'-biphenyl]-2,6-diyl bis(morpholine-4-carboxylate) (C6)

Light white oil, yield 35%; purity, 98.9%. ^1H NMR (400 MHz, CDCl_3) δ 6.74 (s, 2H), 5.34 (s, 1H), 4.60–4.53 (m, 1H), 4.48 (s, 1H), 3.80–3.38 (m, 16H), 2.59–2.50 (m, 2H), 2.50–2.41 (m, 1H), 2.05 (s, 3H), 1.77 (ddd, $J = 19.5, 7.4, 5.1$ Hz, 2H), 1.65 (s, 3H), 1.63–1.54 (m, 2H), 1.53 (s, 3H), 1.35–1.27 (m, 4H), 0.88 (t, $J = 6.9$ Hz, 3H). ^{13}C NMR (101 MHz, CDCl_3) δ 153.3 (2C), 149.9 (2C), 147.6, 141.8, 131.8, 126.6, 124.9, 120.4, 110.9 (2C), 66.6 (2C), 66.5 (2C), 46.1, 44.8 (2C), 44.1 (2C), 38.6, 35.2, 31.5, 30.7, 30.4, 28.8, 23.3, 22.4, 20.2, 14.0. HRMS (ESI) m/z $[\text{M} + \text{Na}]^+$: 563.3087, calcd for $\text{C}_{31}\text{H}_{44}\text{N}_2\text{NaO}_6$: 563.3091.

4.2.9. 6-Hydroxy-5'-methyl-4-pentyl-2'-(prop-1-en-2-yl)-1',2',3',4'-tetrahydro-[1,1'-biphenyl]-2-yl benzyl(methyl)carbamate (C7)

Light yellow oil, yield 41%; purity, 96.6%. ^1H NMR (400 MHz, CDCl_3) δ 7.42–7.30 (m, 5H), 6.87–6.37 (m, 2H), 6.01–5.99 (m, 1H), 5.60 (s, 1H), 4.80–4.32 (m, 4H), 3.59 (s, 1H), 2.97 (s, 3H), 2.61–2.42 (m, 3H), 2.29–2.01 (m, 2H), 1.85–1.44 (m, 10H), 1.35–1.27 (m, 4H), 0.89 (t, $J = 6.8$ Hz, 3H). ^{13}C NMR (101 MHz, CDCl_3) δ 155.2, 154.9, 153.4, 149.9, 147.4, 137.2, 137.1, 128.8, 128.6, 128.1, 127.6, 127.3, 123.7, 119.7, 114.3, 111.0, 100.0, 52.9, 52.7, 38.3, 38.1, 35.5, 31.6, 30.6, 30.5, 23.6, 22.6, 22.5, 20.4, 14.1. HRMS (ESI) m/z $[\text{M} + \text{H}]^+$: 462.3001, calcd for $\text{C}_{30}\text{H}_{40}\text{NO}_3$: 462.3002.

4.2.10. 5'-methyl-4-pentyl-2'-(prop-1-en-2-yl)-1',2',3',4'-tetrahydro-[1,1'-biphenyl]-2,6-diyl bis(benzyl(methyl)carbamate) (C8)

White oil, yield 38%; purity, 99.6%. ^1H NMR (400 MHz, CDCl_3) δ 7.53–7.26 (m, 10H), 6.76 (d, $J = 24.5$ Hz, 2H), 5.41 (s, 1H), 4.87–4.23 (m, 6H), 3.59–3.57 (m, 1H), 2.97 (s, 6H), 2.53 (m, 3H), 2.13–1.89 (m, 2H), 1.84–1.29 (m, 14H), 0.88 (t, $J = 6.1$ Hz, 3H). ^{13}C NMR (101 MHz, CDCl_3) δ 155.1 (2C), 150.4 (2C), 148.1, 141.9, 137.4 (2C), 137.3, 128.9 (4C), 128.8 (4C), 128.3 (2C), 127.8, 127.5, 126.7, 125.4, 111.1, 53.0, 52.8, 46.0, 38.8, 35.5, 34.9, 34.0, 31.9, 30.8, 30.7, 29.2, 23.5, 22.7, 20.3, 14.3. HRMS (ESI) m/z $[\text{M} + \text{Na}]^+$: 631.3502, calcd for $\text{C}_{39}\text{H}_{48}\text{N}_2\text{NaO}_4$: 631.3506.

4.2.11. 6-Hydroxy-5'-methyl-4-pentyl-2'-(prop-1-en-2-yl)-1',2',3',4'-tetrahydro-[1,1'-biphenyl]-2-yl dimethylcarbamate (C9)

Light yellow oil, yield 31%; purity, 98.2%. ^1H NMR (400 MHz, CDCl_3) δ 6.79–6.36 (m, 2H), 6.01 (s, 1H), 5.58 (s, 1H), 4.57 (m, 2H), 3.89–3.52 (m, 1H), 3.02 (dd, $J = 27.4, 4.5$ Hz, 6H), 2.57–2.43 (m, 3H), 2.27–2.02 (m, 2H), 1.86–1.59 (m, 10H), 1.39–1.28 (m, 4H), 0.87 (t, $J = 6.8$ Hz, 3H). ^{13}C NMR (101 MHz, CDCl_3) δ 155.6, 154.9, 150.3, 149.9, 142.7, 141.9, 123.8, 123.7, 114.5, 114.3, 111.1 (2C), 37.9, 36.8, 36.4, 35.4, 35.3, 31.6, 31.4, 30.5, 23.6, 22.5, 22.5, 20.3, 14.0. HRMS (ESI) m/z $[\text{M} + \text{Na}]^+$: 408.2506, calcd for $\text{C}_{24}\text{H}_{35}\text{NNaO}_3$: 408.2509.

4.2.12. 6-Hydroxy-5'-methyl-4-pentyl-2'-(prop-1-en-2-yl)-1',2',3',4'-tetrahydro-[1,1'-biphenyl]-2-yl diethylcarbamate (C10)

Light yellow oil, yield 39%; purity, 98.8%. ^1H NMR (400 MHz, CDCl_3) δ 6.62–6.33 (m, 2H), 6.01 (s, 1H), 5.59 (s, 1H), 4.55 (d, $J = 51.9$ Hz, 2H), 3.60 (s, 1H), 3.52–3.29 (m, 4H), 2.60–2.44 (m, 3H), 2.29–2.01 (m, 2H), 1.86–1.51 (m, 10H), 1.33–1.14 (m, 10H), 0.87 (t,

$J = 6.9$ Hz, 3H). ^{13}C NMR (101 MHz, CDCl_3) δ 155.6, 154.1, 149.8, 147.4, 142.6, 140.0, 123.8, 119.7, 114.5, 114.0, 110.9, 45.3, 41.9, 41.5, 38.1, 35.5, 31.6, 30.6, 30.2, 27.8, 23.6, 22.5, 20.5, 14.4, 14.1, 13.4. HRMS (ESI) m/z $[\text{M} + \text{H}]^+$: 414.2999, calcd for $\text{C}_{30}\text{H}_{40}\text{NO}_3$: 414.3002.

4.2.13. 6-Hydroxy-5'-methyl-4-pentyl-2'-(prop-1-en-2-yl)-1',2',3',4'-tetrahydro-[1,1'-biphenyl]-2-yl piperidine-1-carboxylate (C11)

Light yellow oil, yield 30%; purity, 98.9%. ^1H NMR (400 MHz, CDCl_3) δ 6.60–6.36 (m, 2H), 6.03 (s, 1H), 5.59 (s, 1H), 4.68–4.41 (m, 2H), 3.77–3.27 (m, 5H), 2.61–2.40 (m, 3H), 2.29–2.00 (m, 2H), 1.90–1.47 (m, 16H), 1.36–1.23 (m, 4H), 0.87 (t, $J = 6.9$ Hz, 3H). ^{13}C NMR (101 MHz, CDCl_3) δ 155.5, 153.7, 150.0, 149.9, 142.6, 140.2, 123.8, 119.7, 114.4, 114.1, 111.1, 45.5, 45.1 (2C), 37.9, 35.4, 31.6, 30.6, 30.1, 26.0, 25.5, 24.3 (2C), 23.6, 22.5, 20.2, 14.1. HRMS (ESI) m/z $[\text{M} + \text{Na}]^+$: 448.2818, calcd for $\text{C}_{27}\text{H}_{39}\text{NNaO}_3$: 448.2822.

4.2.14. 6-Hydroxy-5'-methyl-4-pentyl-2'-(prop-1-en-2-yl)-1',2',3',4'-tetrahydro-[1,1'-biphenyl]-2-yl (3-fluorobenzyl) (methyl) carbamate (C12)

Light yellow oil, yield 33%; purity, 97.7%. ^1H NMR (400 MHz, $\text{C}_6\text{D}_5\text{N}$) δ 7.32 (m, 3H), 7.13 (d, $J = 7.9$ Hz, 1H), 6.96–6.78 (m, 2H), 5.72 (s, 1H), 5.06 (m, 2H), 4.82–4.60 (m, 2H), 4.42 (d, $J = 14.7$ Hz, 1H), 3.06 (m, 4H), 2.44 (s, 2H), 2.08–1.79 (m, 7H), 1.66 (m, 3H), 1.48 (s, 2H), 1.14 (s, 5H), 0.74 (s, 3H). ^{13}C NMR (101 MHz, $\text{C}_6\text{D}_5\text{N}$) δ 163.9, 158.1, 155.9, 155.5, 152.4, 149.6, 142.3, 141.7, 131.5, 131.3, 127.3, 123.5, 122.7, 115.4, 115.2, 114.9, 111.7, 52.9, 52.7, 36.1, 35.4, 34.7, 32.1, 31.4, 30.5, 30.4, 24.1, 23.1, 20.1, 14.6. HRMS (ESI) m/z $[\text{M} + \text{Na}]^+$: 502.2717, calcd for $\text{C}_{30}\text{H}_{38}\text{FNNaO}_3$: 502.2718.

4.2.15. 6-Hydroxy-5'-methyl-4-pentyl-2'-(prop-1-en-2-yl)-1',2',3',4'-tetrahydro-[1,1'-biphenyl]-2-yl (3-chlorobenzyl) (methyl) carbamate (C13)

Light yellow oil, yield 30%; purity, 99.6%. ^1H NMR (600 MHz, CDCl_3) δ 7.37–7.28 (m, 1H), 7.26–7.19 (m, 1H), 6.90 (d, $J = 18.0$ Hz, 1H), 6.81 (t, $J = 39.4$ Hz, 1H), 6.64–6.34 (m, 1H), 6.04 (s, 1H), 5.46 (d, $J = 133.2$ Hz, 1H), 4.83–4.36 (m, 4H), 3.92–3.44 (m, 1H), 3.01–2.90 (m, 2H), 2.65–2.47 (m, 3H), 2.30–1.95 (m, 3H), 1.80–1.58 (m, 10H), 1.38–1.28 (m, 5H), 0.88 (t, $J = 5.8$ Hz, 3H). ^{13}C NMR (151 MHz, CDCl_3) δ 154.8, 154.2, 151.2, 149.8, 147.9, 141.9, 139.2, 134.6, 130.0, 129.9, 128.0, 127.8, 127.2, 126.2, 125.3, 122.9, 111.0, 52.5, 45.9, 38.4, 38.2, 35.3, 31.4, 31.3, 30.3, 29.0, 23.8, 22.4, 19.9, 13.9. HRMS (ESI) m/z $[\text{M} + \text{Na}]^+$: 518.2433, calcd for $\text{C}_{30}\text{H}_{38}\text{ClNNaO}_3$: 518.2432.

4.2.16. 6-Hydroxy-5'-methyl-4-pentyl-2'-(prop-1-en-2-yl)-1',2',3',4'-tetrahydro-[1,1'-biphenyl]-2-yl (3-bromobenzyl) (methyl) carbamate (C14)

Light yellow oil, yield 29%; purity, 99.2%. ^1H NMR (400 MHz, $\text{C}_6\text{D}_5\text{N}$) δ 7.74 (s, 1H), 7.59 (s, 1H), 7.43 (s, 1H), 7.35–7.24 (m, 1H), 6.88 (d, $J = 42.2$ Hz, 2H), 5.72 (s, 1H), 5.06 (m, 2H), 4.69 (m, 2H), 4.37 (d, $J = 14.0$ Hz, 1H), 3.08 (m, 4H), 2.45 (s, 2H), 1.95 (m, 6H), 1.68 (m, 3H), 1.48 (s, 3H), 1.15 (s, 5H), 0.75 (d, $J = 4.2$ Hz, 3H). ^{13}C NMR (101 MHz, $\text{C}_6\text{D}_5\text{N}$) δ 158.2, 156.1, 152.3, 149.4, 142.4, 142.3, 141.5, 141.4, 131.6, 131.3, 127.5, 127.3, 123.6, 122.7, 115.9, 113.7, 111.7, 52.8, 52.7, 36.1, 35.4, 34.6, 32.1, 31.5, 31.4, 30.5, 30.4, 24.1, 23.2, 20.2, 14.6. HRMS (ESI) m/z $[\text{M} + \text{H}]^+$: 540.2109, calcd for $\text{C}_{30}\text{H}_{39}\text{BrNO}_3$: 540.2108.

4.2.17. 6-Hydroxy-5'-methyl-4-pentyl-2'-(prop-1-en-2-yl)-1',2',3',4'-tetrahydro-[1,1'-biphenyl]-2-yl (4-fluorobenzyl) (methyl) carbamate (C15)

Light yellow oil, yield 38%; purity, 95.7%. ^1H NMR (400 MHz, $\text{C}_6\text{D}_5\text{N}$) δ 7.49 (s, 2H), 7.17 (s, 2H), 6.97–6.76 (m, 2H), 5.72 (d, $J = 10.1$ Hz, 1H), 4.94 (s, 2H), 4.68 (m, 2H), 4.38 (m, 1H), 3.21–2.88 (m, 4H), 2.44 (s, 2H), 1.94 (m, 6H), 1.66 (m, 3H), 1.48–1.10 (m, 8H),

0.73 (s, 3H), ^{13}C NMR (101 MHz, $\text{C}_6\text{D}_5\text{N}$) δ 163.0, 158.2, 156.0, 155.5, 152.4, 142.3 (2C), 134.8, 130.7 (2C), 127.3, 123.5, 122.7, 116.5, 116.3, 116.1, 111.7, 52.6, 52.5, 36.1, 35.2, 34.5, 32.1, 31.4, 30.4, 24.1, 23.1, 20.1, 14.6. HRMS (ESI) m/z $[\text{M} + \text{Na}]^+$: 502.2716, calcd for $\text{C}_{30}\text{H}_{38}\text{FNNaO}_3$: 502.2718.

4.2.18. 6-Hydroxy-5'-methyl-4-pentyl-2'-(prop-1-en-2-yl)-1',2',3',4'-tetrahydro-[1,1'-biphenyl]-2-yl (4-chlorobenzyl) (methyl) carbamate (C16)

Light yellow oil, yield 35%; purity, 97.0%. ^1H NMR (400 MHz, CDCl_3) δ 7.40–7.27 (m, 2H), 7.27–7.19 (m, 2H), 6.94–6.71 (m, 1H), 6.66–6.37 (m, 1H), 6.06 (s, 1H), 5.47 (d, $J = 86.3$ Hz, 1H), 4.78–4.29 (m, 4H), 3.94–3.42 (m, 1H), 2.97 (t, $J = 4.1$ Hz, 3H), 2.66–2.34 (m, 3H), 2.07 (d, $J = 16.7$ Hz, 1H), 1.83–1.55 (m, 10H), 1.33–1.15 (m, 5H), 0.88 (t, $J = 6.8$ Hz, 3H). ^{13}C NMR (151 MHz, CDCl_3) δ 154.7, 149.8, 147.9, 141.9, 135.6, 133.5, 130.8, 129.5 (2C), 128.9 (2C), 128.8, 128.6, 123.4, 114.3, 113.4, 111.0, 52.3, 45.9, 38.2, 37.5, 35.3, 31.4, 30.4, 30.3, 23.6, 23.4, 22.4, 19.8, 13.9. HRMS (ESI) m/z $[\text{M} + \text{Na}]^+$: 518.2432, calcd for $\text{C}_{30}\text{H}_{38}\text{ClNNaO}_3$: 518.2432.

4.2.19. 6-Hydroxy-5'-methyl-4-pentyl-2'-(prop-1-en-2-yl)-1',2',3',4'-tetrahydro-[1,1'-biphenyl]-2-yl (4-bromobenzyl) (methyl) carbamate (C17)

Light yellow oil, yield 31%; purity, 98.2%. ^1H NMR (400 MHz, CDCl_3) δ 7.55–7.45 (m, 2H), 7.23–7.13 (m, 2H), 6.54 (s, 2H), 6.43 (d, $J = 29.5$ Hz, 0H), 5.95 (s, 1H), 5.58 (d, $J = 10.0$ Hz, 1H), 4.70–4.36 (m, 4H), 3.50 (s, 1H), 2.97 (s, 3H), 2.59–2.41 (m, 3H), 2.13–2.04 (m, 1H), 1.78 (s, 4H), 1.64–1.48 (m, 6H), 1.39–1.23 (m, 5H), 0.88 (t, $J = 6.9$ Hz, 3H). ^{13}C NMR (101 MHz, CDCl_3) δ 155.5, 149.8, 149.7, 142.9, 136.3, 135.2, 131.8 (2C), 129.9 (2C), 129.0, 124.9, 123.5, 121.5, 114.5, 114.3, 110.9, 52.4, 45.3, 38.2, 35.4, 32.2, 31.5, 30.6, 29.8, 26.5, 23.5, 22.6, 20.5, 14.1. HRMS (ESI) m/z $[\text{M} + \text{H}]^+$: 540.2108, calcd for $\text{C}_{30}\text{H}_{39}\text{BrNO}_3$: 540.2108.

4.3. *eeAChE* and *eqBuChE* inhibition assay

Assays were performed on AChE from electric eel (C3389–500UN; Sigma) and BuChE from equine serum (C4290–1KU; Sigma), according to the Ellman's method. The experiment was performed in 48-well plates in a final volume of 500 μL . Each well contained 0.036 U/mL of *eeAChE* or *eqBuChE*, and 0.1 M pH 8 phosphate buffer. They were preincubated for 20 min at different compound concentrations at 37 $^\circ\text{C}$. Then 0.35 mM acetylthiocholine iodide (ACh; A5751-1G; Sigma) or 0.5 mM butyrylthiocholine iodide (BuCh; 20820-1G; Sigma) and 0.35 mM 5,5'-dithiobis(2-nitrobenzoic acid) (DTNB; D8130-1G; Sigma) were added. The DTNB produces the yellow anion 5-thio-2-nitrobenzoic acid along with the enzymatic degradation of ACh or BuCh. Changes in absorbance were measured at 410 nm after 20 min in a PerkinElmer VICTOR Nivo reader. The IC_{50} values were calculated by SPSS 17.0. A control experiment was performed under the same conditions without inhibitor and the blank contained buffer, DMSO, DTNB, and substrate.

4.4. *hAChE* and *hBuChE* inhibition assay

Assays were performed on AChE from human (C1682; Sigma), BuChE from human (B4186; Sigma), 5,5'-dithiobis(2-nitrobenzoic acid) (DTNB; D8130-1G; Sigma), acetylthiocholine iodide (ACh; A5751-1G; Sigma), and butyrylthiocholine iodide (BuCh; 20820-1G; Sigma). Buffer is 0.1 M pH 8 phosphoric acid buffer, Enzyme stock solution was prepared in gelatin (1% in deionized water) and then diluted with water to give 0.125 units per mL. ACh and BuCh iodide solutions were prepared in deionized water to give a final concentration of 3.75 μM . DTNB solution (5 μM) was prepared with

0.1 M pH 8 phosphoric acid buffer. The test compounds were dissolved in DMSO to produce stock solutions with a concentration of 2×10^{-1} M. For each compound, a dilution series of five concentrations (200, 100, 10, 1 and 0.1 μM , diluted with ethanol) was performed. The measurement was conducted using a 96-well plate. Buffer (40 μL), test compounds with a series of concentrations (10 μL), AChE or BuChE (10 μL), and DTNB (20 μL) were successively added into the wells. The mixture was then incubated at 37 $^\circ\text{C}$ for 5 min. Thereafter, 20 μL of ACh or BuCh was added, after which the reaction was initiated. After incubation at 37 $^\circ\text{C}$ for 5 min, the absorption was determined at 412 nm. For the blank value, addition of 10 μL of water replaced the enzyme solution. A plot of percentage of enzyme activity (100% for the reference) versus logarithm of compound concentration was obtained to express the inhibitory activity. The IC_{50} values were calculated by SPSS 17.0.

4.5. Radical scavenging activity (DPPH assay)

The antioxidant capacity of the test compounds were evaluated by DPPH method in which DPPH free radical should be scavenged by antioxidant. Briefly, 150 μL of the compound (200 μM) with 150 μL of DPPH (140 μM) was mixed and incubated in a 96-well plate for 2 h in the dark at 37 $^\circ\text{C}$. The relevant absorbance of the reaction mixture was measured at 520 nm using a microplate reader (PerkinElmer VICTOR Nivo). The reducing percentage (RP) of DPPH was determined by the formula: $\text{RP} = (1 - A_c/A_0) \times 100\%$, where A_c/A_0 are DPPH absorbance in the presence and absence of inhibitors, respectively. Ascorbic acid was used as a standard for DPPH determination.

4.6. Kinetic studies of *eqBuChE* inhibition

Carbamoylation kinetics was measured following the enzyme inhibition protocol. For this purpose, the enzyme was preincubated at 1, 2, 4, 8, 15, 25, 40 and 60 min with five different inhibitor concentrations before the addition of substrate. Plotting the enzyme activity in percentage as a function of time for each inhibitor concentration gave nonlinear time dependent inhibition curves from which k_{obs} was determined by eq (1) (nonlinear regression \rightarrow growth curves \rightarrow exponential plateau).

$$A = A_0 \cdot \exp(-k_{\text{obs}} \cdot t) + A_\infty \quad (1)$$

in which A is the activity of the enzyme at a specific time t , A_0 the activity at $t = 0$, A_∞ the activity at $t = \infty$ and k_{obs} represents the apparent first order rate constant.

Double reciprocal plot of $1/k_{\text{obs}}$ against $1/[I]$ (inhibitor) gave a linear plot from which k_2 and K_d were determined by eq (2).

$$\frac{1}{k_{\text{obs}}} = \frac{k_d}{k_2} \frac{1}{[I]} + \frac{1}{k_2} \quad (2)$$

Determination of the decarbamylation rate constants (k_3), by the analysis of the area under. Follow as:

$$\frac{\text{AUC}_{\text{CE}[t_1,t_2]}}{\text{AUC}_{\text{CE}[t_1,t_2]}} = \frac{1}{k_3} \cdot \frac{cE(t_2) - cE(t_1)}{\text{AUC}_{\text{CE}[t_1,t_2]}} + \frac{K_{\text{obs}}}{k_3} \quad (3)$$

According to formula eq (1), the percentage of enzyme remaining activity (A) is calculated, here we use (E) to indicate the percentage concentration of enzyme activity ($E = A$), then the percentage concentration of enzyme that loses activity after being bound by small carbamate molecules (cE) can be expressed as ($cE = 1 - E$), fit (E) and (cE) with time (t) respectively (Fig. S1), and then use the formula "area under the curve" in the graph-pad to calculate the active enzyme concentration -The area under the time

curve (AUC_E) and the concentration of enzyme that loses activity after being bound—the area under the time curve (AUC_{cE}). In order to reduce the influence of experimental error, we use the most suitable first-order exponential decay formula (eq (1)) to fit the curve, and collect the data of the enzyme and inhibitor incubation time from 15 min to 60 min. A set of minutes to calculate (E) (cE) (AUC_E) and (AUC_{cE}).

Since (t_1) starts from 0 min, $cE(t_1)$ is also 0. It can be found that eq (3) conforms to the characteristics of a linear equation of two variables, and then a straight line can be fitted (Fig. S1) to obtain The X-axis intercept (k_{obs}) and Y-axis intercept (k_{obs}/k_3) of the line. Fit the X-axis intercept (k_{obs}) and Y-axis intercept (k_{obs}/k_3) to a straight line, and obtain (k_3) from the slope (Fig. S1). All kinetic values were determined using the software GraphPad Prism 8.

4.7. Docking-based structural splicing design

On the basis of the structural novelty and the preliminary inhibitory activity, we considered a “fragment-linking” strategy consisting in the chemical linking of these fragments to give higher affinity-binding compounds by additive effect. X-ray crystallographic structures and computational docking were used to guide the fragment linking leading to novel series of BuChE inhibitors. A structure based in silico procedure was applied to discover the binding modes of the active compounds to BuChE enzyme active site. The CDOCKER of Discovery Studio Client v18.1.0 (DS) was conducted to explain SAR of series compounds and further guide the design of more effective and concrete BuChE inhibitors. The ligand binding to the crystal structure of hBuChE with PDB ID: 5LKR was selected as template. All redundant atoms except chain A were deleted and then the protein structure carefully treated in several steps including residue repairing, protonation, and partial charges assignment in CHARMM force field. The target enzyme was prepared with Prepare Protein of DS to ensure the integrity of target. The ligand was processed by Full Minimization of the Small Molecular in DS. The binding pocket was defined by the crystal ligand. Then title compounds were docked into the active site of protein using CDOCKER. The view results of molecular docking were extracted after the program running end, each docking result was analyzed for interaction and their different pose. Those poses with the lowest -CDOCKER_INTERACTION_ENERGY values were regarded as the most stable and picked to analysis binding interactions with target enzyme visualized.

4.7.1. System preparations

The initial structure of hBuChE was retrieved from the RCSB Protein Data Bank (PDB code: 5LKR). Receptor was prepared and missing atoms of residues were fixed by the advanced PDB-Preparation tool in Yinfo Cloud Computing Platform using PDBFixer and the tLEaP module in AmberTools 20. The RESP partial charges of compound **C16** were derived by the Amber antechamber program based on the electrostatic potentials calculated by Gaussian 09 at the B3LYP/6-311G (d,p) level.

4.7.2. Molecular dynamics simulations

The molecular dynamics (MD) simulations were performed in Yinfo Cloud Computing Platform [68] using AmberTools 20 package with AMBER ff19SB and GAFF force fields for hBuChE and compound **C16**, respectively [69,70]. The system was solvated by a truncated octahedron (or cubic) water box using OPC water model with a margin of 10 Å, the net charge was neutralized by (0.15 M of NaCl) sodium ions. Periodic boundary condition (PBC) was used and the net charge neutralized by Na^+ (or Cl^-) ions (or 0.15 M of NaCl). Nonbonded van der Waals interactions were calculated using the Lennard-Jones 12-6 potentials with a 10 Å cutoff, while long-range

electrostatics were treated using the Particle Mesh Ewald (PME) algorithm. The SHAKE algorithm was applied to constrain bonds involving hydrogen atoms. To removed improper atom contacts, the system was first minimized by (1) the 2500 steps of steepest descent and the 2500 steps of the conjugate gradient, under a harmonic constraint of 10.0 kcal/(mol·Å²) on heavy atoms; (2) relaxing the entire system by steepest descent and conjugate gradient each in 10000 steps. And then the system was gradually heated up to 300 K by a 20 ps NVT simulation. The equilibration phase was carried out in two steps: (1) a 200 ps NPT simulation with constraints on heavy atoms followed by (2) a 500 ps NVT simulation without restraint. The temperature and pressure were maintained at 300 K and 1 atm using the Berendsen thermostat and Monte Carlo barostat, with coupling constant and relaxation time of 1 ps. Finally, the system was subjected to a 10 ns NPT simulation with a time step of 2 fs. The root-mean-square deviation (RMSD), root-mean-square fluctuation (RMSF), and hydrogen bonds were analyzed by the Cpptraj module.

4.7.3. MM/PB(GB)SA calculations

The binding free energies were calculated using the Molecular Mechanics Poisson–Boltzmann Surface Area (MM/PBSA) method implemented in AmberTools 20 for 200 snapshots from the MD trajectory. For each snapshot, the free energy was calculated for protein hBuChE, compound **C16**, and the complex hBuChE–**C16** using a single trajectory approach. The total binding free energy was calculated according to the following equation:

$$\Delta G_{\text{bind}} = \Delta G_{\text{complex}} - (\Delta G_{\text{receptor}} - \Delta G_{\text{ligand}})$$

$$\Delta G_{\text{bind}} = \Delta E_{\text{MM}} + \Delta G_{\text{solv}} - T\Delta S$$

$$\Delta E_{\text{MM}} = \Delta E_{\text{vdw}} + \Delta E_{\text{ele}}$$

$$\Delta G_{\text{solv}} = \Delta G_{\text{PB}} + \Delta G_{\text{SA}}$$

where ΔE_{MM} denotes the gas-phase interaction energy between the receptor and the ligand (including van der Waals energy contribution (ΔE_{vdw}) and electrostatic energy contribution (ΔE_{ele}); ΔG_{PB} and ΔG_{SA} are the polar and nonpolar components of the desolvation free energy, respectively; $T\Delta S$ represents the conformational entropy contribution at temperature T. Here, ΔG_{PB} was determined by the Poisson-Boltzmann approximation model, while ΔG_{SA} was estimated based on the solvent accessible surface area model by the method: $\Delta G_{\text{SA}} = \gamma \times \text{SASA} + \beta$, where the values of the constants γ and β were 0.00542 kcal Å⁻² and 0.92 kcal mol⁻¹, respectively. The solvent probe radius and ionic strength were set to be 1.4 Å and 0.15 mM, respectively. The interior and exterior dielectric constant of MM/PBSA calculation systems was 1.0 and 80.0.

4.8. Oil/water partition coefficient assay

Using the classical shake flask method, the oil/water partition coefficient of the compounds was tested. The same amount of oleic phase (noctanol) and aqueous phase (PBS pH 7.4) were mixed. And the mixture was shaken by ultrasonic (400 W, 40 kHz) and allowed to stand for 24 h to obtain a saturated solution of noctanol. An appropriate amount of the compounds was added. After sealing, the test compounds were shaken at 37 °C for 48 h to make it fully equilibrated in the two phases. Then the mixture was measured with a high performance liquid chromatography.

4.9. PAMPA-BBB penetration assay

The ability of the test compound penetrating into the brain was conducted by a parallel artificial membrane permeation assay (PAMPA) for the blood-brain barrier (BBB) based on previous work of Di et al. [58]. Six commercial drugs were used to validate the protocol and purchased from Aladdin Reagents. DMSO and dodecane were obtained from Energy Chemical. Porcine brain lipid (PBL) was purchased from Avanti Polar Lipids. The donor 96-well filter microplate with a PVDF membrane (pore size 0.45 μm) and acceptor indented 96-well microplate were purchased from Millipore. The 96-well UV plate (COSTAR) was obtained from Corning Inc. Commercial drugs and test compounds were initially dissolved in DMSO at a concentration of 20 mg/mL. Subsequently, they were diluted 200-fold with a solution of PBS (pH 7.4 \pm 0.1)/EtOH (70/30, v/v) to give a final concentration of 100 $\mu\text{g}/\text{mL}$. The filter membrane of the donor microplate was coated with 4 μL of PBL in dodecane (20 mg/mL). Then, 200 μL of diluted compound solution was added into the donor wells and 300 μL of PBS/EtOH (70/30, v/v). The donor filter plate was carefully placed on the top of the acceptor plate to form a "sandwich" assembly to make the membrane contact with buffer solution. The sandwich was put undisturbed at 25 $^{\circ}\text{C}$. After incubation for 18 h, the donor plate was carefully removed; the concentrations of test compounds in the donor and acceptor wells were measured with a UV plate spectroscopy reader (PerkinElmer VICTOR Nivo, Finland). Each sample was analyzed at three wavelengths, in at least three independent experiments, in four wells.

4.10. In vitro cytotoxicity assay

Human hepatoblastoma cells HepG2 and human normal liver cells L02 were maintained at 37 $^{\circ}\text{C}$ in a humidified incubator containing 5% CO_2 in DMEM containing 10% fetal bovine serum, 100 U/mL penicillin, and 100 $\mu\text{g}/\text{mL}$ streptomycin. Cell cytotoxicity was evaluated by methyl thiazolyl tetrazolium (MTT) assay. HepG2 cells and L02 cells were inoculated at 1×10^4 cells per well in 96-well plate. After cultured for 24 h, the cells were treated with different compounds which were diluted in DMEM for 24 h. Then 20 μL of 5.0 mg/mL MTT reagent was added into the cells and incubated for 4 h. After 4 h, cell culture was removed and then 150 μL DMSO was added to dissolve the formazan. The optical density was measured at 492 nm (OD_{492}). Cell viability was calculated from three independent experiments. The density of formazan formed in blank group was set as 100% of viability. Cell viability (%) = compound ($\text{OD}_{492}/\text{blank} (\text{OD}_{492}) \times 100\%$.

Blank: cultured with fresh medium only.

Compound: treated with compounds or donepezil.

4.11. Neuroprotection assay

PC12 cells were dispensed into 96-well microtiter plates at a density of 1×10^4 cells/well. Following incubation overnight, cells were treated with a range of CBD and compound **C16** concentrations (0–25 μM) at time zero and maintained for 3 h. Then, the media were replaced by fresh media still containing the drug plus the cytotoxic stimulus represented by 100 μM H_2O_2 that was left for an additional 24 h period. Cell viability was measured after 24 h by using the MTT assay. Briefly, 20 μL of 5.0 mg/mL MTT reagent was added into the cells and incubated for 4 h. After 4 h, cell culture was removed and then 150 μL DMSO was added to dissolve the formazan. The optical density was measured at 492 nm (OD_{492}) on the Biotek Synergy HTX Multi-Mode reader. Results were adjusted considering OD measured in the blank.

4.12. Animal studies

All experiments were performed in accordance with the National Institutes of Health Guide for the Care and Use of Laboratory Animals. The procedures for maintenance and treatment of laboratory animals were approved by the Animal Care and Use Committee of the Anhui Medical University (LLSC20190274). C57BL/6J mice from the Animal Breeding Farm in Anhui Changlinhe Pharmaceutical Technology Co. LTD and male ICR mice from Animal Center of Anhui Medical University (Hefei, China) were used in the MWM task. Six-week-old to eight-week-old male mice (18–24 g) were housed in groups of 10 mice per cage at a room temperature of 22 ± 2 $^{\circ}\text{C}$ under a light/dark (12: 12 h) cycle. The animals had free access to food and water before the tests. The ambient temperature of the room and relative humidity (50%) were kept consistent throughout all of the tests. For the behavioral experiments, the mice were selected at random. Each experimental group consisted of 8–10 mice/dose. The experiments were performed between 08:00 h and 14:00 h. Immediately after the in vivo assays, the mice were euthanized by cervical dislocation. As for scopolamine-induced impairment experiment, CBD and **C16** were tested at a dose 20 mg/kg intraperitoneally in the MWM task. It was suspended in 2% Tween 80 (BioFroxx, Guangzhou) and 0.5% sodium carboxymethyl cellulose (SCR, Shanghai) and was administered 60 min before the behavioral tests. Donepezil HCl (Sigma-Aldrich, Poland) was dissolved in distilled water. In the MWM task, it was tested at 10 mg/kg intraperitoneally. Control mice were given the appropriate amount of vehicle (2% Tween 80 and 0.5% sodium carboxymethyl cellulose). (–)-Scopolamine hydrobromide (Adamas-beta; Shanghai) was used to induce memory impairment in the mice. It was dissolved in distilled water and was administered intraperitoneally at 1 mg/kg, 30 min before the acquisition phase of the MWM tasks. As for the oligomerized $\text{A}\beta_{1-42}$ -induced impairment experiment, 40 male ICR mice were separated into five groups as follows: (i) vehicle (blank control) group (po), (ii) normal saline (icv) as the sham-operation group, (iii) oligomerized $\text{A}\beta_{1-42}$ peptide (10 μg per mouse, icv) model group, (iv) oligomerized $\text{A}\beta_{1-42}$ peptide (10 μg per mouse, icv) + donepezil (15 mg/kg, po) as the positive control group, and (v) oligomerized $\text{A}\beta_{1-42}$ peptide (10 μg per mouse, icv) + **C16** (5 mg/kg, po) as the positive control group. $\text{A}\beta_{1-42}$ peptide was dissolved in DMSO as a 5 mM stock solution and incubated for 24 h at 37 $^{\circ}\text{C}$ in normal saline at a final concentration of 2 mg/mL to induce $\text{A}\beta_{1-42}$ aggregation. The positive and test compounds were suspended in a mixture of DMSO and normal saline (1/99, V/V) before the experiments. The behavioral study is MWM on days 10–15.

4.12.1. In vivo acute toxicity

Compound **C16** was suspended in a mixed solution of DMSO, PEG 400, and saline (10/50/40, v/v/v). Twenty male female mice (20–25 g) were divided into two groups ($n = 10$): control groups and test groups. All mice were fasted overnight and then intragastrically administered with the vehicle or a dosage of 1.0 g/kg of test compound **C16** on the first day. Thereafter, the death, daily behavior, and body weights of mice were monitored during the subsequent 7 days. Body masses of mice were compared between control and test groups and summarized using GraphPad Prism 5.0 software.

4.12.2. In vivo hepatotoxicity studies

In vivo hepatotoxicity was evaluated according to the method previously described in male ICR mice (20–25 g). Compound **C16** was suspended in a mixed solution of DMSO, PEG 400, and saline (10/50/40, v/v/v). A dosage of 30 mg/kg body weight of compound and the same volume of the vehicle were administered

intragastrically (ig). 8, 22, and 36 h after the administration, heparinized serum was collected from the retrobulbar plexus for hepatotoxicity evaluation. The activities of alanine aminotransferase (ALT) and aspartate aminotransferase (AST), two indicators of liver damage, were determined using corresponding assay kits (EF551 and EF550 for ALT, EH027 and EH548 for AST, Wako, Japan). The data were processed using a biochemical analyzer (Hitachi 7020, Japan). After the last collection of retrobulbar blood, mice were sacrificed and livers were taken for morphological studies by the immunohistochemical method. We used an ultrathin semi-automatic microtome (Leica RM2245, Germany) to isolate two 3 mm sections of each liver extending from the hilus to the margin of the left lateral lobe, which was immediately placed in 10% buffered formaldehyde, fixed for 2 days, and embedded together in a paraffin block using a paraffin embedding station (Leica EG1150H, Germany). Subsequently, 5 μ m sections were prepared from those paraffin blocks, deparaffinated, and stained with hematoxylin and eosin or by the method of the periodic acid-Schiff procedure for glycogen.

4.13. Behavioral testing

4.13.1. Scopolamine-induced impairment experiment

MWM Task. The MWM is a circular, plastic, gray-painted pool (diameter, 1.20 m; height, 0.60 m) that is filled with water (up to about 48 cm below the edge, to prevent animals from jumping out) maintained at 23 ± 1 °C. The pool was divided into four equal quadrants (compass locations: NE, NW, SE, SW) using a computerized video tracking system (SMART, version 3.0; Panlab, Spain). An escape platform made of transparent Plexiglas (diameter, 11 cm; height, 47 cm) was positioned at a fixed location (the center of the NW quadrant; i.e., the target quadrant), with this invisible to the swimming animal. It was immersed 1 cm under the surface of the water. During the experiments, the maze was lit with a light intensity of 45 lx. In the spatial acquisition trial (6 consecutive days), the mice were assigned to training sessions (four training sessions per day, sessions held 4 h apart) in which the mice were trained to escape from the water by reaching the hidden platform, the location of which can be identified using distal extra-maze cues attached to the room walls (i.e., A4-sized sheets of black laminated paper with colored geometric symbols), which constitute the navigation points. These visual cues have different colors and dimensions and were kept constant during the whole experiment. The whole experiment was conducted by an experimenter who always remained stationary in a constant location as an additional distal cue for the swimming mice. For each trial, the mouse was placed in the water starting from a different randomly chosen quadrant that did not contain the platform, whereas the platform was always positioned in the same place. If an animal did not find the hidden platform within 60 s, it was gently placed on the platform for 15 s. The time taken to reach the hidden platform (i.e., escape latency time), the distance traveled to reach the hidden platform, the distance in the target (NW) zone, and mean speed were recorded. On day 7 (24 h after the last training session), the platform was removed from the pool and a probe trial was performed (drug-off trial). Each mouse was allowed to swim for 60 s. If a mouse did not find the previous platform position within 60 s, it was given a latency score of 60 s. The latency time to the first crossing of the former platform location (i.e., the target zone), the number of crossings of the target zone, the time spent in the target NW quadrant, the total distance, the distance spent in the NW quadrant, the entries into the NW quadrant, and the mean speed were measured and compared across the experimental groups.

4.13.2. Oligomerized $A\beta_{1-42}$ -induced impairment experiment

As for the oligomerized $A\beta_{1-42}$ -induced impairment experiment, after the behavioral study, all mice were sacrificed and brains were taken to evaluate the amount of total $A\beta_{1-42}$ using the mouse ELISA kit (WuHan HuaMei Biotech Co. Ltd., China). Each brain sample was fully homogenized using a grinder in ten times the amount of PBS (pH = 7.4 ± 0.1) and then centrifuged at a speed of $5000 \times g$ for 5 min. The supernatant was separated for use. The assay procedure was in accordance with the instructions, and the standard curve is presented in the Supporting Information (Fig. S3). The content of brain $A\beta_{1-42}$ was calculated according to the linear regression equation. All values were expressed as means \pm SEM using GraphPad Prism 5.0 software.

4.13.3. Histology examination in hippocampus

For each dose group, nine entire brains separated from three mice were collected to observe CA1 and CA3 regions histopathology in hippocampus. Fresh collected brain was fixed in 4% paraformaldehyde and embedded in paraffin. Paraffin-embedded brains were sectioned on serial coronal sections of 5 μ m thickness. Hematoxylin and eosin (H&E) stained brain sections were analyzed for normal pyramidal neurons hippocampus CA1 and CA3 regions quantification. We performed an image analysis using the Case-Viewer. In each sample, we observe mainly about two fields of each head and the tail and three fields in the middle of the hippocampal CA1 and CA3 regions respectively. Finally, the number of normal pyramidal neuron in all fields-of-view was recorded at magnification $\times 400$. Each normal pyramidal neuron was identified by its shape, size, position and visible nucleus. The reported results in the present study represent the average results for nine fields of CA1 and CA3 regions from three mice in each group.

Declaration of competing interest

The authors declare that they have no known competing financial interests or personal relationships that could have appeared to influence the work reported in this paper.

Acknowledgments

Financial support was provided by Natural Science Foundation of Anhui provincial Department of Education (KJ2019ZD21), and Anhui Provincial Natural Science Foundation (2008085MH261, 2008085MH272). Thanks are given to Dr. Yong-An YANG at Elion Nature Biological Technology Co., Ltd, Nanjing 210038, China for providing the material cannabidiol and its structural identification.

Appendix A. Supplementary data

Supplementary data to this article can be found online at <https://doi.org/10.1016/j.ejmech.2021.113735>.

Abbreviation

$A\beta$	β -amyloid
ACh	acetylcholine;
AChE	acetylcholinesterase
AD	Alzheimer's disease
AEA	anandamide;
AST	aspartate aminotransferase
ALT	alanine aminotransferase
2-AG	2-acyl-glycerol
BBB	blood-brain barrier
BuChE	butyrylcholinesterase
CBD	cannabidiol

CB1 receptor	cannabinoid receptor 1
ChE	cholinesterase
CNS	central nervous system
DPPH	1,1-diphenyl-2-picrylhydrazyl
DTNB	5,5'-dithiobis(2-nitro-benzoic acid)
DS	Discovery Studio Client v18.1.0
EeAChE	<i>Electrophorus electricus</i> AChE
eqBuChE	equine BuChE
FAAH	fatty acid amide hydrolase
GPR55	G protein-coupled receptor 55
HE	hematoxylin–eosin
HPLC	high-performance liquid chromatography
HIA	human intestinal absorption
5HT1A	5-hydroxytryptamine receptor 1A
MD	molecular dynamics
MTT	3-(4,5-dimethylthiazol-2-yl)-2,5-diphenyltetrazolium
PAS	peripheral anionic site;
PAMPA-BBB	parallel artificial membrane permeation assay of BBB
THC	Delta-9-tetrahydrocannabinol
TRPV1	transient receptor potential vanilloid-1

References

- [1] M. Price, A. Comas-Herrera, M. Knapp, M. Guerchet, M. Karagiannidou, The World Alzheimer Report 2016, Alzheimer's Disease International (ADI), London, 2016, pp. 1–131.
- [2] M. Zhou, H. Wang, X. Zeng, P. Yin, J. Zhu, W. Chen, X. Li, L. Wang, L. Wang, Y. Liu, J. Liu, M. Zhang, J. Qi, S. Yu, A. Afshin, E. Gakidou, S. Glenn, V.S. Krish, M.K. Miller-Petrie, W.C. Mountjoy-Venning, E.C. Mullany, S.B. Redford, H. Liu, M. Naghavi, S.I. Hay, L. Wang, C.J.L. Murray, X. Liang, Mortality, morbidity, and risk factors in China and its provinces, 1990–2017: a systematic analysis for the Global Burden of Disease Study 2017, *Lancet* 394 (10204) (2019) 1145–1158.
- [3] S. Mostafavi, C. Gaiteri, S.E. Sullivan, C.C. White, S. Tasaki, J. Xu, M. Taga, H.U. Klein, E. Patrick, V. Komashko, C. McCabe, R. Smith, E.M. Bradshaw, D.E. Root, A. Regev, L. Yu, L.B. Chibnik, J.A. Schneider, T.L. Young-Pearse, D.A. Bennett, P.L. De Jager, A molecular network of the aging human brain provides insights into the pathology and cognitive decline of Alzheimer's disease, *Nat. Neurosci.* 21 (2018) 811–819.
- [4] R. Tundis, M. Bonesi, F. Menichini, M.R. Loizzo, Recent knowledge on medicinal plants as source of cholinesterase inhibitors for the treatment of dementia, *Mini Rev. Med. Chem.* 16 (2016) 605–618.
- [5] M.A. Kamal, P. Klein, W. Luo, Y. Li, H.W. Holloway, D. Tweedie, N.H. Greig, Kinetics of human serum butyrylcholinesterase inhibition by a novel experimental Alzheimer therapeutic, dihydrobenzodioxepine cymserine, *Neurochem. Res.* 33 (2008) 745–753.
- [6] H. Hampel, M.M. Mesulam, A.C. Cuello, M.R. Farlow, E. Giacobini, G.T. Grossberg, A.S. Khachaturian, A. Vergallo, E. Cavado, P.J. Snyder, Z.S. Khachaturian, G. Cholinergic Syst Working, The cholinergic system in the pathophysiology and treatment of Alzheimer's disease, *Brain* 141 (2018) 1917–1933.
- [7] A. Majidi, S. Sadigh-Eteghad, S.R. Aghsan, F. Farajdokht, V.S.M. atandoust, A. Namvaran, J. Mahmoudi, Amyloid-beta, tau, and the cholinergic system in Alzheimer's disease: seeking direction in a tangle of clues, *Rev. Neurosci.* 31 (4) (2020) 391–413.
- [8] S. Xing, Q. Li, B. Xiong, Y. Chen, F. Feng, W. Liu, H. Sun, Structure and therapeutic uses of butyrylcholinesterase: application in detoxification, Alzheimer's disease, and fat metabolism, *Med. Res. Rev.* (2020), <https://doi.org/10.1002/med.21745>.
- [9] N.H. Greig, T. Utsuki, D.K. Ingram, Y. Wang, G. Pepeu, C. Scali, Q.S. Yu, J. Mamczarz, H.W. Holloway, T. Giordano, D. Chen, K. Furukawa, K. Sambamurti, A. Bossi, D.K. Lahiri, Selective butyrylcholinesterase inhibition elevates brain acetylcholine, augments learning and lowers Alzheimer beta-amyloid peptide in rodent, *Proc. Natl. Acad. Sci. Unit. States Am.* 102 (2005) 17213–17218.
- [10] U. Kosak, B. Brus, D. Knez, S. Zakej, J. Trontelj, A. Pislar, R. Sink, M. Jukic, M. Zivin, A. Podkova, F. Nachon, X. Brazzolotto, J. Stojan, J. Kos, N. Coquelle, K. Salat, C.J.-P. olletier, S. Gobec, The magic of crystal structure-based inhibitor optimization: development of a butyrylcholinesterase inhibitor with picomolar affinity and in vivo activity, *J. Med. Chem.* 61 (2018) 119–139.
- [11] Y. Dundar, O. Kuyrukcu, G. Eren, F.S.S. Deniz, T. Onkol, I.E. Orhan, Novel pyridazinone derivatives as butyrylcholinesterase inhibitors, *Bioorg. Chem.* 92 (2019), 103304.
- [12] S.N. Dighe, M. Tippiana, S. van Akker, T.A. Collet, Structure-based scaffold repurposing toward the discovery of novel cholinesterase inhibitors, *ACS Omega* 5 (48) (2020) 30971–30979.
- [13] P. de Andrade, S.P. Mantoani, P.S. Goncalves Nunes, C.R. Magadan, C. Perez, D.J. Xavier, E.T. Sakamoto Hojo, N.E. Campillo, A. Martinez, I. Carvalho, Highly potent and selective aryl-1,2,3-triazolyl benzylpiperidine inhibitors toward butyrylcholinesterase in Alzheimer's disease, *Bioorg. Med. Chem.* 27 (2019) 931–943.
- [14] L. Jing, G. Wu, D. Kang, Z. Zhou, Y. Song, X. Liu, P. Zhan, Contemporary medicinal-chemistry strategies for the discovery of selective butyrylcholinesterase inhibitors, *Drug Discov. Today* 24 (2) (2019) 629–635.
- [15] J. Marikova, A. Ritomska, J. Korabecny, R. Perinova, A. Al Mamun, T. Kucera, E. Kohelova, D. Hulcova, T. Kobrlova, J. Kunes, L. Novakova, L. Cahlikova, Aromatic esters of the crinane amaryllidaceae alkaloid ambelline as selective inhibitors of butyrylcholinesterase, *J. Nat. Prod.* 83 (2020) 1359–1367.
- [16] A. Meden, D. Knez, N. Malinkowska-Racia, X. Brazzolotto, F. Nachon, J. Svete, K. Salat, U. Groselj, S. Gobec, Structure-activity relationship study of tryptophan-based butyrylcholinesterase inhibitors, *Eur. J. Med. Chem.* 208 (2020), 112766.
- [17] J.A. Miles, J.S. Kapure, G.S. Deora, C. Courageux, A. Igert, J. Dias, R.P. McGeary, X. Brazzolotto, B.P. Ross, Rapid discovery of a selective butyrylcholinesterase inhibitor using structure-based virtual screening, *Bioorg. Med. Chem. Lett* 30 (2020), 127609.
- [18] Q. Li, S. Xing, Y. Chen, Q. Liao, B. Xiong, S. He, W. Lu, Y. Liu, H. Yang, Q. Li, F. Feng, W. Liu, Y. Chen, H. Sun, Discovery and biological evaluation of a novel highly potent selective butyrylcholinesterase inhibitor, *J. Med. Chem.* 63 (2020) 10030–10044.
- [19] Z. Zhang, J. Min, M. Chen, X. Jiang, Y. Xu, H. Qin, W. Tang, The structure-based optimization of delta-sultone-fused pyrazoles as selective BuChE inhibitors, *Eur. J. Med. Chem.* 201 (2020), 112273.
- [20] J.A. Miles, B.P. Ross, Recent advances in virtual screening for cholinesterase inhibitors, *ACS Chem. Neurosci.* 12 (2021) 30–41.
- [21] J.M. Roldan-Pena, V. Romero-Real, J. Hicke, I. Maya, A. Franconetti, I. Lagunes, J.M. Padron, S. Petralla, E. Poeta, M. Naldi, M. Bartolini, B. Monti, M.L. Bolognesi, O. Lopez, J.G. Fernandez-Bolanos, Tacrine-O-protected phenolics heterodimers as multitarget-directed ligands against Alzheimer's disease: selective subnanomolar BuChE inhibitors, *Eur. J. Med. Chem.* 181 (2019), 111550.
- [22] M.S. Sadegh, A. Azadi, Z. Izadi, M. Kurd, T. Dara, M. Dibaei, Z.M. Sharif, J.H. Akbari, M. Hamidi, Brain delivery of curcumin using solid lipid nanoparticles and anostructured lipid carriers: preparation, optimization, and pharmacokinetic evaluation, *ACS Chem. Neurosci.* 10 (2019) 728–739.
- [23] E.N. Agbo, S. Gildenhuis, Y.S. Choong, M.J. Mphahlele, G.K. More, Synthesis of furocoumarin-stilbene hybrids as potential multifunctional drugs against multiple biochemical targets associated with Alzheimer's disease, *Bioorg. Chem.* 101 (2020), 103997.
- [24] E.B. Russo, A. Burnett, B. Hall, K.K. Parker, Agonistic properties of cannabidiol at 5-HT1A receptors, *Neurochem. Res.* 30 (2005) 1037–1043.
- [25] E. Manrique-Garcia, S. Zammit, C. Dalman, T. Hemmingsson, S. Andreasson, P. Allebeck, Cannabis, schizophrenia and other non-affective psychoses: 35 years of follow-up of a population-based cohort, *Psychol. Med.* 42 (2012) 1321–1328.
- [26] R. Cooray, V. Gupta, C. Suphioglu, Current aspects of the endocannabinoid system and targeted THC and CBD phytocannabinoids as potential therapeutics for Parkinson's and Alzheimer's diseases: a review, *Mol. Neurobiol.* 57 (2020) 4878–4890.
- [27] L. Cristino, T. Bisogno, V. Di Marzo, Cannabinoids and the expanded endocannabinoid system in neurological disorders, *Nat. Rev. Neurol.* 16 (2020) 9–29.
- [28] Z.X. Xiong, X.F. Muldoon Wang, G.H. Bi, M.I. Damaj, A.H. Lichtman, R.G. Pertwee, E.L. Gardner, Δ^8 -Tetrahydrocannabinavarin has potent anti-nicotinic effects in several rodent models of nicotine dependence, *Br. J. Pharmacol.* 176 (2019) 4773–4784.
- [29] C.D. Schubart, W.A. van Gastel, E.J. Breetvelt, B.S.L. eetz, R.A. Ophoff, I.E. Sommer, R.S. Kahn, M.P. Boks, Cannabis use at a young age is associated with psychotic experiences, *Psychol. Med.* 41 (2010) 1301–1310.
- [30] S. Bhattacharyya, P.D. Morrison, P. Fusar-Poli, R. Martin-Santos, S. Borgwardt, T.C. Winton-Brown, Nosarti, C.M. O'Carroll, M. Seal, P. Allen, M.A. Mehta, J.M. Stone, N. Tunstall, V. Giampietro, S. Kapur, R.M. Murray, A.W. Zuardi, J.A. Crippa, Z. Atakan, P.K. McGuire, Opposite effects of delta-9-tetrahydrocannabinol and cannabidiol on human brain function and psychopathology, *Neuropsychopharmacology* 35 (2010) 764–774.
- [31] da Silva Vanessa Kappel, de Freitas Betânia Souza, Lacerda Garcia Rebeca Carvalho, Tavares Monteiro Ricardo, Eduardo Hallak Jaime, Waldo Zuardi Antônio, S. José Alexandre, Nadja Schröder Crippa, Antiapoptotic effects of cannabidiol in an experimental model of cognitive decline induced by brain iron overload, *transl. Psychiatry* 8 (2018) 176–183.
- [32] C.D. heng, J.K. Low, W. Logge, B. Garner, T. Karl, Chronic cannabidiol treatment improves social and object recognition in double transgenic appsw/ps1e9 mice, *Psychopharmacology (Berlin)* 231 (15) (2014) 3009–3017.
- [33] G. Watt, K. Shang, J. Zieba, J. Olaya, H. Li, B. Garner, T. Karl, Chronic treatment with 50 mg/kg cannabidiol improves cognition and moderately reduces A β 40 levels in 12-month-old male A β PPsw/PS1 Δ E9 transgenic mice, *J. Alzheimers Dis.* 74 (2020) 937–950.
- [34] A. Gururajan D.T. Malone, Does cannabidiol have a role in the treatment of schizophrenia? *Schizophr. Res.* 176 (2016) 281–290.
- [35] C. Wojciech, P.D. Wojciech, B. Fredrik, A.R. Iexander, S. Jan, E. Inna, Component of cannabis, cannabidiol, as a possible drug against the cytotoxicity of A β (31–35) and A β (25–35) peptides: an investigation by molecular dynamics and well-tempered metadynamics simulations, *ACS Chem. Neurosci.* 12 (4) (2021)

- 660–674.
- [36] L. Casares, J.D. Unciti-Broceta, M.E. Prados, C.D. aprioglio, D. Mattoteia, M. Higgins, G. Appendino, Din A.T. kova-Kostova, E. Muñoz, L. de la Vega, Isomeric O-methyl cannabidiolquinones with dual BACH1/NRF2 activity, *Redox Biol* 37 (2020), 101689.
- [37] H. Li, Y. Liu, Ti D. an, L. Tian, C. Liang, Overview of cannabidiol (cbd) and its analogues: structures, biological activities, and neuroprotective mechanisms in epilepsy and alzheimer's disease, *Eur. J. Med. Chem.* 192 (2020), 112163.
- [38] A.K. Ghosh, M. Brindisi, Organic carbamates in drug design and medicinal chemistry, *J. Med. Chem.* 58 (2015) 2895–2940.
- [39] A.C. Galasiti Kankanamalage, Y. Kim, A.D. Rathnayake, K.R. Alliston, M.M. Butler, S.C. Cardinale, T.L. Bowlin, W.C. Groutas, K.O. Chang, Design, synthesis, and evaluation of novel prodrugs of transition state inhibitors of norovirus 3CL protease, *J. Med. Chem.* 60 (2017) 6239–6248.
- [40] B. Li, S. Cai, Y.A. Yang, S.C. Chen, R. Chen, J.B. Shi, X.H. Liu, W.J. Tang, Novel unsaturated glycyrrhetic acids derivatives: design, synthesis and anti-inflammatory activity, *Eur. J. Med. Chem.* 139 (2017) 337–348.
- [41] J. Jampilek, K. Brychtova, Azone analogues: classification, design, and transdermal penetration principles, *Med. Res. Rev.* 32 (2012) 907–947.
- [42] M. Vettorazzi, E. Angelina, S. Lima, T. Gonc, J. Otevreil, P. Marvanova, T. Padrtova, P. Mokry, B.P. obal, L.M. Acosta, A. Palma, J. Cobo, J. Bobalova, J. Collei, I. Malik, S. Alvarez, S. Spiegel, J. Jampilek, R.D. Enriz, An integrative study to identify novel scaffolds for sphingosine kinase 1 inhibitors, *Eur. J. Med. Chem.* 139 (2017) 461–481.
- [43] A. Imramovsky, M. Pesko, J. Monreal-Ferriz, K. Kralova, J. Vinsova, J. Jampilek, Photosynthesis-inhibiting efficiency of 4-chloro-2-(chlorophenylcarbamoyl) phenyl alkylcarbamates, *Bioorg. Med. Chem. Lett* 21 (2011) 4564–4567.
- [44] Jiri Kos, Nevin Eoghan, Soral Michal, Kushkevych Ivan, Gonc Tomas, Bobal Pavel, Kollar peter, coffey aidan, O'mahony jim, liptaj, tibor, kralova katarina, jampilek josef, synthesis and antimicrobial properties of ring-substituted 6-hydroxynaphthalene-2-carboxanilides, *Bioorg. Med. Chem.* 23 (2015) 2035–2043.
- [45] S. Pospisilova, J. Kos, H. Michnova, I. Kapustikova, S.T. trharsky, M. Oravec, A.M. Moricz, J. Bakonyi, T. Kauerova, P. Kollar, A. Cizek, J. Jampilek, Synthesis and spectrum of biological activities of novel N-arylcinnamamides, *Int. J. Mol. Sci.* 19 (2018), 2318.
- [46] P. Bar-On, C.B. Millard, M. Harel, H. Dvir, A. Enz, S.J.L. ussman, I. Silman, Kinetic and structural studies on the interaction of cholinesterases with the anti-Alzheimer drug rivastigmine, *Biochemistry* 41 (2002) 3555–3564.
- [47] Pizova Hana, Havelkova Marketa, Bobal Pavel, Stepankova Sarka, Kauerova Tereza, Andrzej Bak, Kollar Peter, Kozik Violetta, Oravec Michal, Imramovsky Ales, Jampilek Josef, Proline-based carbamates as cholinesterase inhibitors, *Molecules* 22 (2017) 1969.
- [48] F. Pollastro, D. Caprioglio, P. Marotta, A.S. Moriello, L. De Petrocellis, O. Tagliatalata-Scafati, G. Appendino, Iodine-promoted aromatization of p-menthane-type phytocannabinoids, *J. Nat. Prod.* 81 (2018) 630–633.
- [49] S.N. Dighe, G.S. Deora, E. De la Mora, F. Nachon, S. Chan, M.O. Parat, X. Brazzolotto, B.P. Ross, Discovery and structure-activity relationships of a highly selective butyrylcholinesterase inhibitor by structure-based virtual screening, *J. Med. Chem.* 59 (2016) 7683–7689.
- [50] G.L. Qiu, S.S. He, S.C. Chen, B. Li, H.H. Wu, J. Zhang, W.J. Tang, Design, synthesis and biological evaluation of tricyclic pyrazolo 1,5-c 1,3 benzoxazin-5(5H)-one scaffolds as selective BuChE inhibitors, *J. Enzym. Inhib. Med. Chem.* 33 (2018) 1506–1515.
- [51] R. Dash, M. Junaid, S. Mitra, A.M. rifuzzaman, S.M.Z. Hosen, Structure-based identification of potent VEGFR-2 inhibitors from in vivo metabolites of a herbal ingredient, *J. Mol. Model.* 25 (2019) 98.
- [52] M. Marta, F. Gatta, M. Pomponi, Physostigmine analogs anticholinesterases: effects of the lengthening of the N-carbamic chain on the inhibition kinetics, *Biochim. Biophys. Acta Protein Struct. Mol. Enzymol.* 1120 (1992) 262–266.
- [53] E. Sawatzky, S. Wehle, B. Kling, J. Wendrich, G. Bringmann, C.A. Sotriffer, J. Heilmann, M. Decker, Discovery of highly selective and nanomolar carbamate-based butyrylcholinesterase inhibitors by rational investigation into their inhibition mode, *J. Med. Chem.* 59 (2016) 2067–2082.
- [54] S. Montanari, L. Scalvini, M. Bartolini, F. Belluti, S. Gobbi, V. Andrisano, A. Ligresti, V. Di Marzo, S. Rivara, M. Mor, A. Bisi, A. Rampa, Fatty acid amide hydrolase (FAAH), acetylcholinesterase (AChE), and butyrylcholinesterase (BuChE): networked targets for the development of carbamates as potential anti-alzheimer's disease agents, *J. Med. Chem.* 59 (2016) 6387–6406.
- [55] M. Hoffmann, C. Stiller, E. Endres, M. Scheiner, S. Gunesch, C. Sotriffer, T. Maurice, M. Decker, Highly selective butyrylcholinesterase inhibitors with tunable duration of action by chemical modification of transferable carbamate units exhibit pronounced neuroprotective effect in an alzheimer's disease mouse model, *J. Med. Chem.* 62 (2019) 9116–9140.
- [56] B.D. Freudenthal, W.A. Beard, L. Perera, D.D. Shock, T. m Ki, T. Schlick, S.H. Wilson, Uncovering the polymerase-induced cytotoxicity of an oxidized nucleotide, *Nature* 517 (2015) 635–639.
- [57] Y. Xu, Z. Zhang, X. Jiang, X. Chen, Z. Wang, H. Alsulami, H.L. Qin, W.J. Tang, Discovery of δ -sultone-fused pyrazoles for treating Alzheimer's disease: design, synthesis, biological evaluation and SAR studies, *Eur. J. Med. Chem.* 181 (2019), 111598.
- [58] L. Di, E.H. Kerns, I.F. Bezar, S.L. Petusky, Y. Huang, Comparison of blood-brain barrier permeability assays: in situ brain perfusion, MDR1-MDCKII and PAMPA-BBB, *J. Pharm. Sci.* 98 (2009) 1980–1991.
- [59] W.J. Tang, J. Wang, X. Tong, J.B. Shi, X.H. Liu, J. Li, Design and synthesis of celastrol derivatives as anticancer agents, *Eur. J. Med. Chem.* 95 (2015) 166–173.
- [60] S.N. Dighe, G.S. Deora, De E. la Mora, F. Nachon, S. Chan, M.O. Parat, X. Brazzolotto, B.P. Ross, Discovery and structure-activity relationships of a highly selective butyrylcholinesterase inhibitor by structure-based virtual screening, *J. Med. Chem.* 59 (2016) 7683–7689.
- [61] M. Wu, J. Ma, L. Ji, M. Wang, Z. Li, Design, synthesis, and biological evaluation of rutacearpine derivatives as multitarget-directed ligands for the treatment of alzheimer's disease, *Eur. J. Med. Chem.* 177 (2019) 198–211.
- [62] M.J. ehla, S.H. Deibel, F.J. araji, T. Saito, T.C. Saido, M.H. Mohajerani, R.J. McDonald, Looking beyond the standard version of the Morris water task in the assessment of mouse models of cognitive deficits, *Hippocampus* 29 (2019) 3–14.
- [63] L.E. Berkowitz, R.E. Harvey, E. Drake, S.M. Thompson, B.J. Clark, Progressive impairment of directional and spatially precise trajectories by TgF344-Alzheimer's disease rats in the Morris Water Task, *Sci. Rep.* 8 (2018), 16153.
- [64] T.E. Evans, H.H.H. Adams, S. Licher, F.J. Wolters, A. van der Lugt, M.K. Ikram, M.J. O'Sullivan, M.W. Vernooij, M.A. Ikram, Subregional volumes of the hippocampus in relation to cognitive function and risk of dementia, *Neuroimage* 178 (2018) 129–135.
- [65] J.F.O. da Cruz, A. Busquets-Garcia, Z.Z. hao, M. Varilh, G. Lavanco, L. Bellocchio, L. Robin, A. Cannich, F. Julio-Kalajzic, T. Leste-Lasserre, M. Maitre, F. Drago, G. Marsicano, E. Soria-Gomez, Specific hippocampal interneurons shape consolidation of recognition memory, *Cell Rep.* 32 (2020), 108046.
- [66] P.T. Nelson, C.D. Smith, E.L. Abner, B.J. Wilfred, W.-X. Wang, J.H. Neltner, B.M. aker, D.W. Fardo, R.J. Kryscio, S.W. Scheff, G.A. Jicha, K.A. Jellinger, Van L.J. Eldik, F.A. Schmitt, Hippocampal sclerosis of aging, a prevalent and high-morbidity brain disease, *Acta Neuropathol.* 126 (2013) 161–177.
- [67] H. Zhang, H. Kuang, Y. Luo, S. Liu, L. Meng, P.Q. ang, R. Fan, Low-dose bisphenol A exposure impairs learning and memory ability with alterations of neuromorphology and neurotransmitters in rats, *Sci. Total Environ.* 697 (2019), 134036.
- [68] A Friendly and Versatile Cloud Computing Platform for Biomedical, Material, and Statistical Researches. <https://cloud.yinfotek.com/>.
- [69] J. Wang, R.M. Wolf, J.W. Caldwell, P.A. Kollman, D.A. Case, Development and testing of a general AMBER force field, *J. Comput. Chem.* 25 (2004) 1157–1174.
- [70] T. Darden, D. York, L. Pedersen, Particle mesh Ewald: an N-log(N) method for Ewald sums in large systems, *J. Chem. Phys.* 98 (1993) 10089–10092.